J. Mech. Phys. Solids 175 (2023) 105273

Contents lists available at ScienceDirect

Journal of the Mechanics and Physics of Solids

journal homepage: www.elsevier.com/locate/jmps

Actin based motility unveiled: How chemical energy is converted into motion

C. Bonanno [a,b], M. Serpelloni [a,c], M. Arricca [a,c], R.M. McMeeking [a,d,e], A. Salvadori [a,c,*]

[a] The Mechanobiology Research Center, UNIBS, Brescia 25123, Italy
[b] Department of Civil, Environmental, Architectural Engineering and Mathematics, Università degli Studi di Brescia, via Branze 43, Brescia 25123, Italy
[c] Department of Mechanical and Industrial Engineering, Università degli Studi di Brescia, via Branze 38, Brescia 25123, Italy
[d] Materials and Mechanical Engineering Departments, University of California, Santa Barbara, CA 93106, USA
[e] INM - Leibniz Institute for New Materials, Campus D2 2, Saarbruecken 66123, Germany

ARTICLE INFO

Keywords:
Mechanobiology
Actin-based motility
Cell motility
Multiphysics models
Finite strains thermo-mechanics of continua

ABSTRACT

Actin-based motility is a complex process in which the actin-polymerization is the primary force-generating motor machinery. It can produce protrusive forces through actin filaments polymerization and cross-link during lamellipodia protrusion in migrating cells and it is responsible for the intracellular motion of certain pathogens in infected host cells. We propose a multi-physics model for actin-based motility, stemming from continuity equations that account for the actin chemical kinetics. Thermodynamic restrictions are identified, moving from the multiplicative decomposition of the deformation gradient into chemical and elastic parts. Constitutive theory and chemical kinetics are prescribed to finally write governing equations for the multi-physics problem. The field equations are solved numerically with the finite element method. As a proof of concept, a one-dimensional model for actin-based motility of bacteria pathogens is studied.

1. Introduction

The chemo-mechanical motor of several biological systems is a polymerization process that converts chemical energy into mechanical work. The chief component in this activity is actin, a multi-functional protein forming filament in the cell cytoskeleton that is capable of generating protrusive forces when polymerization occurs in close proximity to a barrier or to a load (Theriot, 2000). External impulses of a chemical or mechanical nature trigger a chemical reaction, which converts the monomeric form of actin, G-actin, into a polymerized branched-filamentous form, F-actin Blanchoin et al. (2014). The actin filament assembly may be a bundle (in filopodia, the Thyone sperm, and Chlamydomonas) or a cross-linked web (in lamellipodia, pseudopodia, and comet tails) (Theriot, 2000; Kadzik et al., 2020). Upon polymerization, the cross-linked network acts against the plasma membrane, a pathogenic bacterium or an endosome, pushing them forward and promoting directional motility (Hu and Papoian, 2010). We claim that the phase change of monomeric actin to a cross-linked network of filament causes a *volumetric expansion*, which ultimately converts chemical energy into motion.

The notion of volumetric expansion is common to many types of motors. In steam engines, for example, a fuel is burned and heat is used to boil water and produce steam. Heat is converted into motion when the steam expands and pushes a piston. Similarly, chemical energy is converted into motion when the polymerization of G-actin into a cross-linked network gives rise to volumetric

* Corresponding author at: Department of Mechanical and Industrial Engineering, Università degli Studi di Brescia, via Branze 38, Brescia 25123, Italy.
E-mail address: alberto.salvadori@unibs.it (A. Salvadori).

https://doi.org/10.1016/j.jmps.2023.105273
Received 6 November 2022; Received in revised form 24 February 2023; Accepted 12 March 2023
Available online 17 March 2023

expansion and protrusive forces: the most studied biological events in this context are the protrusion of lamellipodia in migrating cells and the propulsion of certain intracellular pathogens (Svitkina, 2018).

Lamellipodia are flat cellular protrusions at the leading edge of cells, where actin is organized in a bidimensional dendritic array of branched filaments (Le Clainche and Carlier, 2008). Branched actin filaments are generated beneath the plasma membrane by external signal responsive WASP-Arp2/3 machinery and kept functioning by a set of regulatory proteins (Le Clainche and Carlier, 2008; Carlier and Pantaloni, 1997). Those binding proteins control actin turnover and filament elongation, mediate the initiation of new filaments as branches on pre-existing filaments and promote (de)branching and (de)polymerization, thus regulating the mechanical response of lamellipodia (Pollard, 2016; Borisy and Svitkina, 2000; Pollard and Borisy, 2003). Upon mechanical loading, actin networks change density, power, and efficiency, showing load adaptation and reorganization during motility. Microscopically, this is reflected by a change of filament number and an altered geometry. Macroscopically, it leads to a variation of network stiffness and resistance to mechanical failure. This reveals a viscoelastic behavior of lamellipodia that exhibit a "memory" of their mechanical history (Bieling et al., 2016; Mueller et al., 2017).

The polymerization motor is essential also to the virulence of several pathogens, e.g., *Listeria monocytogenes, Shigella, Ricketssia, Mycobacterium* and *Burkholderia* (Goldberg, 2001; Radoshevich and Cossart, 2018; Ortega et al., 2019). To enhance the spread of infection (Lamason and Welch, 2017), they have evolved the ability to manipulate the motility mechanisms of the host cell at multiple stages of infection. After escaping into the cytosol, they induce actin polymerization on their surface and use filament assembly to power intracellular actin-based motility (ABM), thus generating *actin comet tails* that trail the moving bacteria (Choe and Welch, 2016). The *actin comet tail* resembles a simplified lamellipodium and the bacterial surface imitates the plasma membrane at the leading edge of a moving cell (Theriot, 2000; Pantaloni et al., 2001). Each of these bacteria separately and convergently have developed a different mechanism to utilize the cellular actin assembly machinery (Goldberg, 2001) and they have evolved distinctive proteins that take the role of an external signal that triggers the polymerization of cellular actin (Pizarro-Cerdá et al., 2012). This group of proteins binds and activates one or more of the components of a cellular actin assembly pathway, thereby inducing a cascade of activation of all of the effector molecules, with the end result being actin nucleation, polymerization, and cross-linking (Goldberg, 2001).

Uncountable papers have been published on the ABM biology, whereas few mathematical models provided insights into ABM mechanisms. Most of them concern the microstructural machinery of the pulling action of *single* filaments. In recent years there have been several notable publications that propose models for pathogen trajectories (Shenoy et al., 2007; Kang et al., 2010), for substrate-cell interactions (Li et al., 2010; Gong et al., 2018), for the movement of *Listeria* (Lin et al., 2010), for studying spatial actin densities (Raz-Ben Aroush et al., 2017), for the simulations of the dynamic behavior of actin-based cytoskeletal networks (Gong et al., 2019) and for coupling mechanisms of cell adhesion, contraction and spreading (Vernerey and Farsad, 2014).

Lamellipodia protrusion dynamics has been modeled in Hu and Papoian (2010) through a microscopic physico-chemical computational framework, which accounts for the biochemical regulation processes and the interactions between actin filaments and the flexible lipid membrane. A profound investigation was carried out on how growing filaments generate forces to push the membrane, concluding that *polymerizing actin filaments apply the needed force on membrane, pushing it forward*. The interactions between the cytoskeleton and the membrane was modeled by a steric repulsion between the membrane and the actin filaments. A triangulated membrane model was proposed more recently in Ni and Papoian (2021), accounting for membrane–filaments interactions and membrane's elastic properties. Ni and Papoian developed an excluded volume interaction via repulsion between filament's tip and a meshwork triangle, where essentially every point on the surface of the membrane interacts with the tip. This notion, named as responsible for the cell motility, differs from the hypothesis of the present note, that attributes the motion to a volumetric expansion. Carlsson (2001, 2003) developed a stochastic simulation method to study the growth of branched networks against rigid obstacles. Rubinstein et al. (2005) performed multiscale, two-dimensional numerical modeling of a crawling cell using a finite element approach. Atilgan et al. (2005) performed theoretical and computational studies of the morphology of the lamellipodium. A mechanobiochemical model was recently presented by Murphy and Madzvamuse (2020), who considered the actin filament network as a viscoelastic and contractile gel. The mechanical properties were modeled by a force balancing equation for the displacements, while the pressure and contractile forces are driven by *actin and myosin dynamics*, in turn depicted by a system of reaction–diffusion equations on a moving cell domain. Such an approach shows similarities to the one pursued in the present manuscript.

We propose a thermodynamically consistent continuum-mechanics formulation, stemming from continuity equations that account for actin chemical kinetics. The model manifests itself in macroscopic descriptors of biochemical and biological details of the relevant processes, thereby resulting in sufficient generality to be appropriate for several biological systems. Since the mechanical motor function of actin-based motility is performed by the F-actin network generated during a chemical reaction, we consider (see Section 3) a multiplicative decomposition of the deformation gradient $\boldsymbol{F}$ into elastic and polymerization parts $\boldsymbol{F}^e$ and $\boldsymbol{F}^c$, respectively, with the latter taken to be isotropic. The *polymerization map* $\boldsymbol{F}^c$ represents the local distortion of the material neighborhood of a point due to the phase change of monomeric actin to a network of filaments and vice-versa. Although differing in the details of its development and in applications, our theory is based on Chester and Anand (2010). The splitting of the deformation gradient takes into account two experimental evidences: the first is the reorganization of G-actin into F-actin networks (and vice-versa), which causes a volumetric deformation because monomers and cross-linked filaments have different molar volumes; the second is the deformation of the F-actin network subjected to external loads.

The paper is organized as follows. Balance equations for conservation of mass, linear, and angular momentum are introduced in Section 4. The law of mass action for actin phase transformation is defined in Section 5. Balance of energy, entropy, and thermodynamic restrictions are introduced in Section 6. Subsequently, in Section 7, we provide constitutive theories having

Table 1
Scalar, vector, and tensor notation.

Variables and values	Reference configuration	Current configuration
scalar	a_R	a
vector	$\vec{A}$	$\vec{a}$
2-nd order tensor	$\boldsymbol{A}$	$\boldsymbol{a}$

consistent phenomenological specifications for mass fluxes and mechanical stress, as well as for the evolution of inelastic processes. Moreover, coupling of chemical kinetics to all other processes is analyzed, pinpointing when phenomena can be categorized as not rate limiting and therefore that can be modeled as instantaneous. Governing equations are summarized in Section 8 and subsequently written in weak form. As a representative example of application of the theory, in Section 9 we introduce a one-dimensional model for actin-based motility of intracellular pathogens.

2. Nomenclature

2.1. Notation

The notation for scalars, vectors, and tensors is summarized in Table 1. Lowercase fonts denote $\vec{vector}$ and $\boldsymbol{tensor}$ fields in the current configuration, whereas uppercase letters are used for referential $\vec{VECTOR}$ and $\boldsymbol{TENSOR}$ fields. A different notation holds for scalar fields, consistently with Gurtin et al. (2010), which are denoted with a subscript $_R$ in the reference configuration. The reason for this choice is that uppercase letters either denote parameters (as per the Young modulus, E globular G or filamentous F actin), or the different customary scalar fields (as per temperature T versus time t).

2.2. Operators

- the symbol $\mathrm{div}\,[\ ]$ and $\nabla\,[\ ]$ denote the divergence and gradient operators in the current configuration
- the symbols $\mathrm{Div}\,[\ ]$ and $\mathrm{Grad}\,[\ ]$ denote the same operators in the reference configuration
- the symbol $\cdot$ denotes the scalar product, either for vectors or for tensors (double index contraction)
- the symbol $\frac{\mathrm{d}\phi}{\mathrm{d}t}$ denotes the *total* derivative of a field ϕ (scalar, vector, or tensor) with respect to time t, while $\frac{\partial\phi}{\partial t}$ denotes the *partial* derivative of a field ϕ (scalar, vector, or tensor) with respect to time t.

3. Kinematics

Consider a continuum body Ω, as in Fig. 1. Denote with $\vec{X}$ the material point in the reference configuration Ω_R. A *motion* of Ω_R is a smooth function $\vec{\chi}(\vec{X},t)$ that assigns to each material point at time t a location

$$\vec{x} = \vec{\chi}(\vec{X},t)\,,$$

which is referred to as the spatial point occupied by $\vec{X}$ at time t (Gurtin et al., 2010). We will name *deformation* $\vec{\chi}_t$ a motion at a *fixed* time t

$$\vec{\chi}_t(\vec{X}) = \vec{\chi}(\vec{X},t)\,.$$

The deformation gradient is denoted as usual with

$$\boldsymbol{F} = \mathrm{Grad}\left[\,\vec{\chi}_t\,\right], \tag{1}$$

where the mathematical restriction $J = \det[\,\boldsymbol{F}\,] > 0$ holds. The F-actin crosslinked network is considered as having a greater molar volume than monomeric G-actin. We represent this as a continuum dilatation of the actin in which the dilated configuration, the F-actin network, is a mixture of cytosol and polymerized actin monomers. In view of this, we base our model on a multiplicative decomposition of the deformation gradient

$$\boldsymbol{F} = \boldsymbol{F}^e\boldsymbol{F}^c\,, \tag{2}$$

which splits the total deformation gradient into two contributions: a purely chemical contribution $\boldsymbol{F}^c$ and a purely mechanical contribution $\boldsymbol{F}^e$:

- $\boldsymbol{F}^c(\vec{X},t)$ is called the *polymerization tensor* and is the local distortion of the material neighborhood of a point due to the volumetric swelling (de-swelling) of the material due to the phase change of actin, after polymerization from monomeric to a network of filaments and vice-versa (Serpelloni et al., 2021).
- $\boldsymbol{F}^e(\vec{X},t)$ is called elastic distortion and is the local distortion of the material neighborhood of a point due to the elasticity of the network.

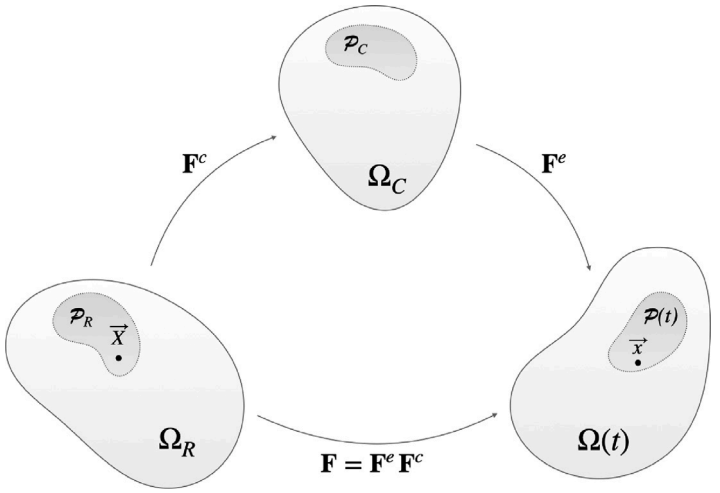

Fig. 1. The reference Ω_R, the intermediate Ω_C and the deformed $\Omega(t)$ configuration. The arrows indicate the mapping properties of the linear transformations $\boldsymbol{F}$, $\boldsymbol{F}^e$, and $\boldsymbol{F}^c$.

$\boldsymbol{F}^c(\vec{X},t)$ is defined as

$$\boldsymbol{F}^c = \lambda^c\,\mathbb{1}\,, \tag{3}$$

with

$$\lambda^c > 0\,, \qquad \det\left[\boldsymbol{F}^c\right] = J^c = \lambda^{c3}\,, \qquad \frac{1}{J^c}\frac{\mathrm{d}J^c}{\mathrm{d}t} = \frac{3}{\lambda^c}\frac{\mathrm{d}\lambda^c}{\mathrm{d}t}\,, \tag{4}$$

and λ^c is the swelling stretch. In view of definition (3), the decomposition (2) leads to a multiplicative decomposition for the left Cauchy–Green tensor, too:

$$\boldsymbol{C}(\vec{X},t) = \boldsymbol{C}^e\,\boldsymbol{C}^c\,, \tag{5}$$

with the polymerization and elastic factors

$$\boldsymbol{C}^c = \boldsymbol{F}^{c\mathrm{T}}\boldsymbol{F}^c = J^{c\,2/3}\,\mathbb{1}\,, \qquad \boldsymbol{C}^e = \boldsymbol{F}^{e\mathrm{T}}\boldsymbol{F}^e = J^{c-2/3}\,\boldsymbol{C}\,, \tag{6}$$

respectively. The Green–Langrange strain tensor $\boldsymbol{E}$ and its elastic counterpart, defined as

$$\boldsymbol{E}^e = \frac{1}{2}\left(\boldsymbol{C}^e - \mathbb{1}\right), \tag{7}$$

are related by the identities

$$\boldsymbol{E} = J^{c\,2/3}\,\boldsymbol{E}^e + \frac{1}{2}\left(J^{c\,2/3} - 1\right)\mathbb{1}\,, \tag{8}$$

and

$$\frac{\mathrm{d}\,\boldsymbol{E}}{\mathrm{d}t} = \frac{1}{3}\left(J^{c-1/3}\,\frac{\mathrm{d}\,J^c}{\mathrm{d}t}\boldsymbol{C}^e\right) + \left(J^{c\,2/3}\,\frac{\mathrm{d}\,\boldsymbol{E}^e}{\mathrm{d}t}\right). \tag{9}$$

The spatial velocity gradient is defined as usual as

$$\boldsymbol{l}(\vec{x},t) = \nabla\left[\vec{v}(\vec{x},t)\right] = \frac{\mathrm{d}\,\boldsymbol{F}}{\mathrm{d}t}\,\boldsymbol{F}^{-1}\,, \tag{10}$$

and the following tensors

$$\boldsymbol{l}^e = \frac{\mathrm{d}\,\boldsymbol{F}^e}{\mathrm{d}t}\,\boldsymbol{F}^{e^{-1}}\,, \qquad \boldsymbol{l}^c = \frac{\mathrm{d}\,\boldsymbol{F}^c}{\mathrm{d}t}\,\boldsymbol{F}^{c^{-1}} \tag{11}$$

are defined in Ω and Ω_c, respectively. It holds

$$\boldsymbol{l} = \boldsymbol{l}^e + \boldsymbol{F}^e\,\boldsymbol{l}^c\,\boldsymbol{F}^{e^{-1}}. \tag{12}$$

The linear field $\boldsymbol{l}(\vec{x},t)$ can be split into the rate of deformation tensor $\boldsymbol{d}(\vec{x},t)$ and the spin (vorticity tensor) $\boldsymbol{w}(\vec{x},t)$

$$\boldsymbol{l}^c = \boldsymbol{d}^c + \boldsymbol{w}^c\,, \tag{13a}$$

$$\boldsymbol{l}^e = \boldsymbol{d}^e + \boldsymbol{w}^e. \tag{13b}$$

From Eq. (3) and (4) the following transformations hold

$$\boldsymbol{w}^c = \boldsymbol{0}\,, \qquad \boldsymbol{l}^c = \boldsymbol{d}^c = \frac{1}{3\,J^c}\,\frac{\mathrm{d}\,J^c}{\mathrm{d}t}\,\mathbb{1}\,, \qquad \frac{\mathrm{d}\,J^c}{\mathrm{d}t} = J^c\,\mathrm{tr}\left[\,\boldsymbol{d}^c\,\right]. \tag{14}$$

In view of Eq. (12) and (14), $\boldsymbol{l} = \boldsymbol{l}^e + \boldsymbol{l}^c$ holds.

In the realm of viscoelasticity (Simo and Hughes, 1998; Holzapfel, 2001), the deformation gradient $\boldsymbol{F}^e$ is frequently defined as a multiplicative decomposition of the deformation gradient into volumetric $\boldsymbol{F}^{e^v}$ and isochoric $\boldsymbol{F}^{e^i}$ factors

$$\boldsymbol{F}^e = \boldsymbol{F}^{e^v}\,\boldsymbol{F}^{e^i}\,, \tag{15}$$

with volumetric factor $\boldsymbol{F}^{e^v} = J^{e\,1/3}\,\mathbb{1}$ completely identified by the determinant of $\boldsymbol{F}^e$ and for the isochoric factor $\det\left[\,\boldsymbol{F}^{e^i}\,\right] = 1$. These results lead to similar relationships to those summarized above.

4. Balance laws

The reorganization of monomeric subunits into a network through polymerization induces a local change in volume, which is captured in a continuum based framework by a polymerization tensor. The process is reversible, and a volume decrement occurs upon depolymerization.

Such a mechanism also requires the presence of a cytosol, capable of filling all interstitials during network expansion and to retreat upon shrinkage. Furthermore, the cytosol brings monomeric units into the proximity of the signal, thus stimulating the polymerization process. In the present version of our model, we do not provide the cytosol with any mechanical capability, other than a viscous drag on the F-actin network. The cytosol, though, is considered as a medium through which species can flow and diffuse.

Accordingly, at a point $\vec{X} \in \Omega_R$ we can idealize the coexistence of G actin and a polymer network in the cytosol, each of those two species being able to flow according to mass balances. Mechanical strength and stiffness at $\vec{X} \in \Omega_R$ are provided by the polymerized network; at all locations at which no network is present, the balance of momentum reduces to the trivial null identity. At all other locations, linear and angular momentum rule the transmission of loads through interaction of the polymeric skeleton and the cytosol.

4.1. Mass balance

The interplay between the monomeric (G) and network (F) of actin in the cytosol is described as a chemical reaction

$$\mathrm{G} \underset{k_b}{\overset{k_f}{\rightleftarrows}} \mathrm{F}\,, \tag{16}$$

which portrays how many moles of G-actin are converted into F-actin network and vice-versa by the rate of the reaction (16), denoted with $w^{(16)}$. The parameters k_b and k_f denote the backward and forward reaction rate parameters. We define a mole of F-actin network as the result of the polymerization of a mole of G-actin monomers.

Define

$$c_a(\vec{x},t)\,, \qquad \text{with} \quad a = G, F\,, \tag{17}$$

as the molarity (moles per unit volume) reckoned per unit volume of the current configuration. If necessary, molarity of species can be rephrased in terms of density, multiplying by molecular mass (m_G or m_F).

The mass balance equations of species G and F in the polymerized configuration, schematized in Fig. 2, localize as — omitting the dependency upon $\vec{x}$ and t

$$\frac{\partial c_G}{\partial t} + \mathrm{div}\left[\,c_G\,\vec{v}_{adv}\,\right] + \mathrm{div}\left[\,\vec{h}_G\,\right] + w^{(16)} = s_G\,, \tag{18a}$$

$$\frac{\partial c_F}{\partial t} + \mathrm{div}\left[\,c_F\,\vec{v}_{adv}\,\right] + \mathrm{div}\left[\,\vec{h}_F\,\right] - w^{(16)} = 0. \tag{18b}$$

The mass flux vector $\vec{h}_a$, expressed in terms of moles per unit area per unit time, is the transport in addition to advection, so that $\vec{h}_a = c_a(\vec{v}_a - \vec{v}_{adv})$; s_G is the rate in moles at which the G-actin is generated by cells. Since F-actin network production results only from the chemical reaction (16), the source term s_F is null.

The mass balance equation can be defined in the reference configuration at point $\vec{X}$ and time t. Every specific quantity per unit volume transforms as the density

$$c_{a_R}(\vec{X},t) = c_a(\,\vec{x}(\vec{X},t),t\,)\,J(\vec{X},t)\,, \tag{19a}$$

$$w^{(16)}_R(\vec{X},t) = J(\vec{X},t)\,w^{(16)}(\vec{x}(\vec{X},t),t)\,, \tag{19b}$$

$$s_{G_R}(\vec{X},t) = J(\vec{X},t)\,s_G(\,\vec{x}(\vec{X},t),t\,)\,, \tag{19c}$$

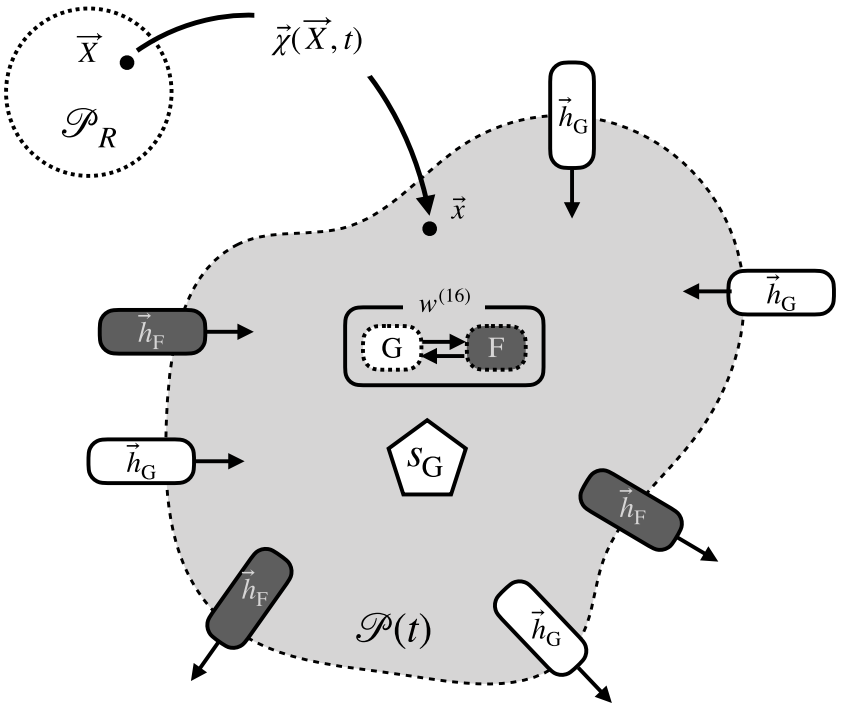

Fig. 2. Schematic representation of the mass balance on an advecting cytosol $\mathcal{P}(t)$. A straightforward application of Reynold's theorem leads to Eq. (18).

while, taking advantage of Nanson' s relationship, surface fluxes transform as

$$\vec{H}_a(\vec{X},t) = J\,\boldsymbol{F}^{-1}\,\vec{h}_a(\vec{x}(\vec{X},t),t)\,, \tag{20}$$

where $\vec{H}_a(\vec{X},t)$ is the reference flux vector. The mass balance equations in the reference configuration eventually read

$$\frac{\partial c_{G_R}}{\partial t} + \mathrm{Div}\left[\vec{H}_G\right] + w_R^{(16)} = s_{G_R}\,, \tag{21a}$$

$$\frac{\partial c_{F_R}}{\partial t} + \mathrm{Div}\left[\vec{H}_F\right] - w_R^{(16)} = 0. \tag{21b}$$

4.2. Balance of momentum

As already mentioned, in this model the mechanical strength is provided by the polymerized network. For this reason, in the referential local form the balance of linear momentum reads

$$\mathrm{Div}\,[\,\boldsymbol{P}\,] + \vec{B} = \frac{\mathrm{d}\,\rho_{F_R}\,\dot{\vec{\chi}}}{\mathrm{d}t}\,, \qquad \vec{X} \in \Omega_R \tag{22}$$

with $\vec{B}$ denoting external body forces per unit reference volume in the material representation, $\dot{\vec{\chi}}$ denoting the referential F-actin network advection velocity and ρ_{F_R} denoting the referential density of actin network. $\boldsymbol{P}$ is the nominal stress tensor (first Piola–Kirchhoff stress tensor), obeying the symmetry condition

$$\boldsymbol{P}\boldsymbol{F}^T = \boldsymbol{F}\boldsymbol{P}^T\,, \tag{23}$$

which is the balance of angular momentum. Among the external forces acting on the F-actin network, the cytosol viscous drag forces are included, that act opposite to the relative motion of F-actin network.

5. Chemical kinetics: mass action

5.1. Swelling factor

We assume that the G-actin is partially transformed into F-actin network by the reaction (16); hence at every point $\vec{X} \in \Omega_R$ at time t, two phases G and F coexist. In the initial condition the reference state is defined to be pure monomeric G-actin and in the absence of any mechanical effect the volume of a neighborhood at $\vec{X}$ evolves as

$$\mathrm{d}v = \mathrm{d}v_R + (mol_F)\,\Omega_F\,, \tag{24}$$

with $\Omega_F = (\omega_F - \omega_G)$. ω_a denotes the molar volume of a-species (volume of the a-mole, presumed to be constant), which takes a different value for each species (ω_G and ω_F).

From Eq. (24), the change in volume per unit reference volume can be written as

$$J^c(\vec{X},t) = \frac{\mathrm{d}v}{\mathrm{d}v_R} = 1 + c_{F_R}(\vec{X},t)\,\Omega_F\ , \tag{25}$$

with c_{F_R} depicting the referential concentration of F-actin network and J^c representing the swelling factor, entirely due to polymerization. From Eq. (25), we can write

$$\frac{\mathrm{d}\,J^c}{\mathrm{d}t} = \Omega_F\ \frac{\mathrm{d}\,c_{F_R}}{\mathrm{d}t}\ . \tag{26}$$

5.2. Signal for polymerization and delay for depolymerization

The mass action law for the reaction (16) in the current configuration reads

$$w^{(16)}(\vec{x},t) = k_f\ \frac{\vartheta_G}{1-\vartheta_G} - k_b\ \frac{\vartheta_F}{1-\vartheta_F}\ , \tag{27}$$

with k_b and k_f the backward and forward reaction rate parameters,

$$\vartheta_a(\vec{x},t) = \frac{c_a(\vec{x},t)}{c_a^{max}(\vec{x},t)} \qquad \text{with} \quad a = G, F\ , \tag{28}$$

and c_a^{max} the saturation limit for every a-species. Taking advantage of Eq. (19a) and (19b), Eq. (27) writes in the reference configuration as

$$w_R^{(16)}(\vec{X},t) = k_{f_R}\ \frac{\vartheta_{G_R}}{1-\vartheta_{G_R}} - k_{b_R}\ \frac{\vartheta_{F_R}}{1-\vartheta_{F_R}}\ , \tag{29}$$

with ϑ_{a_R} denoting the ratio

$$\vartheta_{a_R}(\vec{X},t) = \frac{c_{a_R}(\vec{X},t)}{c_{a_R}^{max}(\vec{X},t)}\ , \qquad \text{with} \quad a = G, F. \tag{30}$$

As discussed in Serpelloni et al. (2022), two paradigmatic cases shall be considered for the relationship between the saturation concentration in the reference and in the current configuration. Here it is assumed that the maximum number of molecules per unit volume is invariant: this case occurs when the volume occupied by each unit species is invariant, and species can relocate to occupy eventual volumetric expansions of the hosting material. Under this assumption, $c_{a_R}^{max}(\vec{X},t) = c_a^{max}(\vec{x},t)$, while $k_{f_R} = k_f$ and $k_{b_R} = k_b$ *far from saturation*.

The F-actin network formation is induced by a signaling pathway (Pizarro-Cerdá et al., 2012; Cameron et al., 2000), that is strictly related to an external activator (e.g., proteins on the pathogens surface for bacteria or external mechanical or chemical gradients for cells). For the sake of simplicity, the precise details of signaling processes are ignored and the signaling pathway can be identified as an external activation that triggers the polymerization of G-actin, as done in Deshpande et al. (2006). For this reason, the forward reaction rate parameter k_f is considered as

$$k_f = C(\vec{X},t)\,k_f^*\ , \tag{31}$$

where k_f^* is a constant and $C(\vec{X},t)$ represents the activation signal that triggers actin polymerization.

The network depolymerization is also dependent on external cues; whereas biological studies are still insufficiently detailed, we include all environmental factors (such as the mechanical stress in the network, among others) into a phenomenological descriptor, a time delay τ from the onset of polymerization, which corresponds to the notion of the half-life of filaments, introduced in Cameron et al. (2000). For this reason, the backward reaction rate parameter is defined as follows:

$$\begin{aligned} &k_b = 0 \qquad && \text{if} \quad c_{F_R}(\vec{X},t-\tau) = 0\ , \\ &k_b = k_b^* \qquad && \text{otherwise}\ . \end{aligned} \tag{32}$$

Two circumstances occur:

- the depolymerization does not take part at point $\vec{X}$ of the cell in which the concentration of F-actin network at time $t-\tau > 0$ was null, namely everywhere when $t-\tau \le 0$ or where G-actin had not been polymerized at time $t-\tau$ yet. This implies that $k_b = 0$ and it is consistent with considering that each filament has a lifetime, during which no depolymerization occurs;
- the depolymerization does take part at positions $\vec{X}$ of the cell where F-actin network was already present at time $t-\tau$. This implies that $k_b = k_b^*$ with $k_b^* \neq 0$ and it entails that filaments start to depolymerize a period of time τ after their polymerization began.

6. Thermodynamics

6.1. Energy balance

Consider a thermodynamic continuum that can exchange energy with the surroundings due to mechanical, heat, and mass transfer. The first law of thermodynamics (energy balance) rules the transformation from one type of energy involved in the thermodynamic process into another. Considering an arbitrary material region $\mathcal{P}_R$, the referential global energy balance reads

$$\frac{\mathrm{d}\,\mathcal{K}}{\mathrm{d}t} + \frac{\mathrm{d}\,\mathcal{U}}{\mathrm{d}t} = \mathcal{W}_u + \mathcal{Q}_u + \mathcal{T}_u \,, \tag{33}$$

with $\mathcal{K}$ the kinetic energy, $\mathcal{U}$ the internal energy, $\mathcal{W}_u$ the mechanical external power, $\mathcal{Q}_u$ the thermal power and $\mathcal{T}_u$ the power due to mass transfer. The individual contributions read

$$\frac{\mathrm{d}\,\mathcal{K}}{\mathrm{d}t} = \int_{\mathcal{P}_R} \frac{1}{2}\frac{\mathrm{d}\,\rho_{F_R}\,\dot{\vec{\chi}}\cdot\dot{\vec{\chi}}}{\mathrm{d}t}\,\mathrm{d}v_R, \tag{34a}$$

$$\frac{\mathrm{d}\,\mathcal{U}}{\mathrm{d}t} = \int_{\mathcal{P}_R} \frac{\mathrm{d}\,u_R}{\mathrm{d}t}\,\mathrm{d}v_R \,, \tag{34b}$$

$$\mathcal{W}_u = \int_{\partial\mathcal{P}_R} \dot{\vec{\chi}}\cdot\boldsymbol{P}\,\vec{N}\,\mathrm{d}a_R + \int_{\mathcal{P}_R}\dot{\vec{\chi}}\cdot\vec{B}\,\mathrm{d}v_R \,, \tag{34c}$$

$$\mathcal{Q}_u = \int_{\mathcal{P}_R} s_{q_R}\,\mathrm{d}v_R - \int_{\partial\mathcal{P}_R}\vec{Q}\cdot\vec{N}\,\mathrm{d}a_R \,, \tag{34d}$$

$$\mathcal{T}_u = \int_{\mathcal{P}_R} {}^{u}\mu_G\, s_{G_R}\,\mathrm{d}v_R - \int_{\partial\mathcal{P}_R} {}^{u}\mu_F\,\vec{H}_F\cdot\vec{N} + {}^{u}\mu_G\,\vec{H}_G\cdot\vec{N}\,\mathrm{d}a_R \,, \tag{34e}$$

where $\dot{\vec{\chi}}$ represents the referential velocity, u_R the internal energy density per unit volume, s_{q_R} the heat source per unit reference volume and unit time generated into region $\mathcal{P}_R$ of the body, $\vec{Q}$ the heat flux vector per unit reference surface area and unit time and $\vec{N}$ the outward unit normal to the reference surface. $\vec{H}_a$ and s_{G_R} are defined in paragraph 4.1 and ${}^{u}\mu_a$ denotes the change in specific energy provided by a unit supply of moles of a-species.

From Eq. (34c) we can rewrite the mechanical external power $\mathcal{W}_u$ as

$$\mathcal{W}_u = \int_{\mathcal{P}_R} \boldsymbol{P}\cdot\frac{\mathrm{d}\,\boldsymbol{F}}{\mathrm{d}t} + \frac{1}{2}\frac{\mathrm{d}\,\rho_{F_R}\,\dot{\vec{\chi}}\cdot\dot{\vec{\chi}}}{\mathrm{d}t}\,\mathrm{d}v_R \,, \tag{35}$$

and using the standard divergence theorem for Eq. (34d) and (34e) and mass balance for the two species, the referential global energy balance eventually takes the form

$$\begin{aligned}\int_{\mathcal{P}_R}\frac{\mathrm{d}\,u_R}{\mathrm{d}t}\,\mathrm{d}v_R = \int_{\mathcal{P}_R} \boldsymbol{P}\cdot\frac{\mathrm{d}\,\boldsymbol{F}}{\mathrm{d}t} + s_{q_R} - \mathrm{Div}\left[\vec{Q}\right] + \left({}^{u}\mu_G - {}^{u}\mu_F\right)\,w_R^{(16)} \\ + {}^{u}\mu_G\frac{\partial c_{G_R}}{\partial t} - \vec{H}_G\cdot\mathrm{Grad}\left[{}^{u}\mu_G\right] + {}^{u}\mu_F\frac{\partial c_{F_R}}{\partial t} - \vec{H}_F\cdot\mathrm{Grad}\left[{}^{u}\mu_F\right]\,\mathrm{d}v_R.\end{aligned} \tag{36}$$

6.2. Entropy imbalance

Considering an arbitrary material region $\mathcal{P}_R$, the referential global entropy imbalance reads

$$\frac{\mathrm{d}\,\mathcal{S}}{\mathrm{d}t} - \mathcal{Q}_\eta - \mathcal{T}_\eta \geq 0 \,, \tag{37}$$

with $\mathcal{S}$ the net internal entropy, $\mathcal{Q}_\eta$ the entropy per unit time due to heat transfer and $\mathcal{T}_\eta$ the entropy per unit time due to mass transfer. The individual contributions read

$$\frac{\mathrm{d}\,\mathcal{S}}{\mathrm{d}t} = \int_{\mathcal{P}_R}\frac{\mathrm{d}\,\eta_R}{\mathrm{d}t}\,\mathrm{d}v_R \,, \tag{38a}$$

$$\mathcal{Q}_\eta = \int_{\mathcal{P}_R}\frac{1}{T}\,s_{q_R}\,\mathrm{d}v_R - \int_{\partial\mathcal{P}_R}\frac{1}{T}\,\vec{Q}\cdot\vec{N}\,\mathrm{d}a_R \,, \tag{38b}$$

$$\mathcal{T}_\eta = \int_{\mathcal{P}_R} {}^{\eta}\mu_G\, s_{G_R}\,\mathrm{d}v_R - \int_{\partial\mathcal{P}_R} {}^{\eta}\mu_G\,\vec{H}_G\cdot\vec{N} + {}^{\eta}\mu_F\,\vec{H}_F\cdot\vec{N}\,\mathrm{d}a_R \,, \tag{38c}$$

where η_R represents the internal entropy density per unit of volume and ${}^{\eta}\mu_a$ denotes the change in specific entropy provided by a unit supply of moles of a-species.

Multiplying Eq. (37) by T and taking advantage of Eq. (36) to re-write the term $-s_{q_R} + \mathrm{Div}\left[\vec{Q}\right]$, after some algebra Eq. (37) in the global form reads

$$\begin{aligned}\int_{\mathcal{P}_R} T\frac{\mathrm{d}\,\eta_R}{\mathrm{d}t} - \frac{\mathrm{d}\,u_R}{\mathrm{d}t} + \boldsymbol{P}\cdot\frac{\mathrm{d}\,\boldsymbol{F}}{\mathrm{d}t} + \mu_G\frac{\partial c_{G_R}}{\partial t} + \mu_F\frac{\partial c_{F_R}}{\partial t} - \vec{H}_G\cdot\mathrm{Grad}\left[\mu_G\right] + \\ - \vec{H}_F\cdot\mathrm{Grad}\left[\mu_F\right] - A^{(16)}\,w_R^{(16)}\,\mathrm{d}v_R \geq 0 \,,\end{aligned} \tag{39}$$

having defined $\mu_a = {}^{u}\mu_a - T\,{}^{\eta}\mu_a$ for the a-species and $A^{(16)} = \mu_F - \mu_G$.

6.3. Helmholtz free energy

The specific *Helmholtz free energy* per unit referential volume, which is a suitable thermodynamic potential in continuum mechanics, is defined through a Legendre transformation, in the state variables[1] c_{a_R}, $\boldsymbol{E}$ and some kinematic internal variable $\boldsymbol{\xi}$, as

$$\psi_R = u_R - T\,\eta_R. \tag{40}$$

Taking advantage of Eq. (40) and using the derivative of the *Helmholtz free energy* with respect to time at thermal equilibrium

$$\frac{\mathrm{d}\,\psi_R}{\mathrm{d}t} = \frac{\mathrm{d}\,u_R}{\mathrm{d}t} - T\,\frac{\mathrm{d}\,\eta_R}{\mathrm{d}t} - \frac{\mathrm{d}\,T}{\mathrm{d}t}\,\eta_R = \frac{\mathrm{d}\,u_R}{\mathrm{d}t} - T\,\frac{\mathrm{d}\,\eta_R}{\mathrm{d}t}\,, \tag{41}$$

we re-write Eq. (39) as

$$\int_{\mathcal{P}_R} \frac{\mathrm{d}\,\psi_R}{\mathrm{d}t} - \boldsymbol{S}\cdot\frac{\partial\,\boldsymbol{E}}{\partial t} - \mu_F\,\frac{\partial c_{F_R}}{\partial t} - \mu_G\,\frac{\partial c_{G_R}}{\partial t} + A^{(16)}\,w_R^{(16)} + \vec{H}_G\cdot\mathrm{Grad}\left[\,\mu_G\,\right] + \vec{H}_F\cdot\mathrm{Grad}\left[\,\mu_F\,\right]\;\mathrm{d}v_R \le 0\,, \tag{42}$$

where an alternative expression for the stress power, with the second Piola–Kirchhoff stress tensor $\boldsymbol{S}$, is employed. The total time derivative of $\psi_R = \psi_R\left(c_{G_R}, c_{F_R}, \boldsymbol{E}, \boldsymbol{\xi}\right)$ reads

$$\frac{\mathrm{d}\,\psi_R}{\mathrm{d}t} = \left.\frac{\partial\psi_R}{\partial\boldsymbol{E}}\right|_{c_{F_R},c_{G_R},\xi}\cdot\frac{\partial\boldsymbol{E}}{\partial t} + \left.\frac{\partial\psi_R}{\partial c_{G_R}}\right|_{c_{F_R},\boldsymbol{E},\xi}\frac{\partial c_{G_R}}{\partial t} + \left.\frac{\partial\psi_R}{\partial c_{F_R}}\right|_{c_{G_R},\boldsymbol{E},\xi}\frac{\partial c_{F_R}}{\partial t} + \left.\frac{\partial\psi_R}{\partial\boldsymbol{\xi}}\right|_{c_{F_R},c_{G_R},\boldsymbol{E}}\cdot\frac{\partial\boldsymbol{\xi}}{\partial t}. \tag{43}$$

Substituting Eq. (43) into Eq. (42), the Clausius–Duhem inequality arises

$$\begin{aligned}\int_{\mathcal{P}_R} \left(\frac{\partial\psi_R}{\partial\boldsymbol{E}} - \boldsymbol{S}\right)\cdot\frac{\partial\boldsymbol{E}}{\partial t} + \left(\frac{\partial\psi_R}{\partial c_{F_R}} - \mu_F\right)\frac{\partial c_{F_R}}{\partial t} + \left(\frac{\partial\psi_R}{\partial c_{G_R}} - \mu_G\right)\frac{\partial c_{G_R}}{\partial t} + \\ - \boldsymbol{\chi}\cdot\frac{\partial\boldsymbol{\xi}}{\partial t} + \vec{H}_G\cdot\mathrm{Grad}\left[\,\mu_G\,\right] + \vec{H}_F\cdot\mathrm{Grad}\left[\,\mu_F\,\right] + A^{(16)}\,w_R^{(16)}\;\mathrm{d}v_R \le 0\,,\end{aligned} \tag{44}$$

which can be localized at $\vec{X} \in \mathcal{P}_R$ since it holds for any arbitrary subpart $\mathcal{P}_R$.

6.4. Intermediate configuration

We can rewrite the internal power in the intermediate configuration as

$$\begin{aligned}\int_{\mathcal{P}_R} \boldsymbol{S}\cdot\frac{\mathrm{d}\,\boldsymbol{E}}{\mathrm{d}t}\;\mathrm{d}v_R &= \int_{\mathcal{P}_R} \boldsymbol{P}\cdot\frac{\mathrm{d}\,\boldsymbol{F}}{\mathrm{d}t}\;\mathrm{d}v_R = \\ &= \int_{\mathcal{P}_C} \boldsymbol{P}^e\cdot\frac{\mathrm{d}\,\boldsymbol{F}^e}{\mathrm{d}t} + \boldsymbol{M}^e\cdot\boldsymbol{l}^c\;\mathrm{d}v_c \\ &= \int_{\mathcal{P}_C} \boldsymbol{S}^e\cdot\frac{\mathrm{d}\,\boldsymbol{E}^e}{\mathrm{d}t} + \frac{1}{3J^c}\frac{\mathrm{d}\,J^c}{\mathrm{d}t}\,\mathrm{tr}\left[\,\boldsymbol{M}^e\,\right]\;\mathrm{d}v_c\,,\end{aligned} \tag{45}$$

where we have defined

$$\boldsymbol{S}^e = J^e\boldsymbol{F}^{e^{-1}}\boldsymbol{\sigma}\boldsymbol{F}^{e^{-\mathrm{T}}}\,,\qquad \boldsymbol{P}^e = J^e\boldsymbol{\sigma}\boldsymbol{F}^{e^{-\mathrm{T}}} = \boldsymbol{F}^e\boldsymbol{S}^e\,,\qquad \boldsymbol{M}^e = J^e\boldsymbol{F}^{e^{\mathrm{T}}}\boldsymbol{\sigma}\boldsymbol{F}^{e^{-\mathrm{T}}} = \boldsymbol{C}^e\boldsymbol{S}^e \tag{46}$$

as the elastic second and first Piola–Kirchhoff tensors and the elastic Mandel stress tensor. The detailed derivation of the Eq. (45) is given in Appendix.

6.5. Thermodynamic restrictions

Since the Clausius–Duhem inequality (44) holds for every admissible process, the following thermodynamic prescriptions in the reference configuration arise through the Coleman-Noll procedure

$$\boldsymbol{S} = \left.\frac{\partial\psi_R}{\partial\boldsymbol{E}}\right|_{c_{G_R},c_{F_R},\xi}\,, \tag{47a}$$

$$\mu_G = \left.\frac{\partial\psi_R}{\partial c_{G_R}}\right|_{c_{F_R},\boldsymbol{E},\xi}\,, \tag{47b}$$

$$\mu_F = \left.\frac{\partial\psi_R}{\partial c_{F_R}}\right|_{c_{G_R},\boldsymbol{E},\xi}\,, \tag{47c}$$

[1] State variables are all referential fields. Accordingly, their total and partial derivatives with respect to time coincide. For this reason, we will use the notation of partial derivative henceforth for all state variables.

and the dissipation inequality in the reference configuration

$$\underbrace{-\chi \cdot \frac{\partial \xi}{\partial t}}_{\text{inelastic}} + \underbrace{\vec{H}_G \cdot \text{Grad}\left[\mu_G\right] + \vec{H}_F \cdot \text{Grad}\left[\mu_F\right]}_{\text{mass transport}} + \underbrace{w_R^{(16)} A^{(16)}}_{\text{chemical}} \leq 0 \tag{48}$$

holds, where we have denoted

$$\chi = -\frac{\partial \psi_R}{\partial \xi} \,. \tag{49}$$

Adopting the Curie principle, inequality (48) can be written as

$$-\chi \cdot \frac{\partial \xi}{\partial t} \leq 0 \,, \tag{50a}$$

$$\vec{H}_F \cdot \text{Grad}\left[\mu_F\right] + \vec{H}_G \cdot \text{Grad}\left[\mu_G\right] \leq 0 \,, \tag{50b}$$

$$w_R^{(16)} A^{(16)} \leq 0 \,, \tag{50c}$$

where ξ and χ represent the internal flux variables and their energy-conjugate forces, respectively, and $A^{(16)}$ is deduced to be the chemical affinity of the reaction.

To satisfy the inequality (50b), the flows of G-actin monomers and F-actin network, $\vec{H}_G$ and $\vec{H}_F$, are linearly correlated to the gradient of their chemical potentials, $\text{Grad}\left[\mu_G\right]$ and $\text{Grad}\left[\mu_F\right]$, as follows

$$\vec{H}_G = -\boldsymbol{M}_{G_R} \text{Grad}\left[\mu_G\right] \,, \tag{51a}$$

$$\vec{H}_F = -\boldsymbol{M}_{F_R} \text{Grad}\left[\mu_F\right] \,, \tag{51b}$$

where $\boldsymbol{M}_{G_R}$ and $\boldsymbol{M}_{F_R}$ are positive definite mobility tensors of the monomeric G-actin and the network of F-actin, respectively. They are taken as

$$\boldsymbol{M}_{G_R}(c_{G_R}) = \mathbb{m}_{G_R} c_{G_R}^{max} \vartheta_{G_R} \left(1 - \vartheta_{G_R}\right) \mathbb{1} \,, \tag{52a}$$

$$\boldsymbol{M}_{F_R}(c_{F_R}) = \mathbb{m}_{F_R} c_{F_R}^{max} \vartheta_{F_R} \left(1 - \vartheta_{F_R}\right) \mathbb{1} \,, \tag{52b}$$

with $\mathbb{m}_{G_R} > 0$ and $\mathbb{m}_{F_R} > 0$ the *mobilities* respectively of the monomeric G-actin and the network of F-actin. More complex laws, of Maxwell–Stefan type (Ganser et al., 2019), can be used for the G and F-actin flows in place of (51). The inequality (50c) is a priory satisfied by the mass action law (29).

7. Constitutive theory

The Helmholtz free energy density ψ_R can be represented by an additive decomposition

$$\psi_R(c_{G_R}, c_{F_R}, \boldsymbol{E}, \xi) = \psi_R^{diff}(c_{G_R}, c_{F_R}) + \psi_R^{el}(c_{F_R}, \boldsymbol{E}) + \psi_R^{in}(c_{F_R}, \boldsymbol{E}, \xi) \,, \tag{53}$$

which separates the diffusive contribution ψ_R^{diff}, the elastic contribution ψ_R^{el}, and the inelastic counterpart ψ_R^{in}.

7.1. Mechanical contribution

Following Holzapfel (2001), we will define visco-elastic materials based on the multiplicative decomposition (15), using tensors $\boldsymbol{E}^{e^v}$ and $\boldsymbol{E}^{e^i}$. Specifically, the free energy for visco-elastic materials will be defined as follows

$$\psi_R^{el}(c_{F_R}, \boldsymbol{E}) + \psi_R^{in}(c_{F_R}, \boldsymbol{E}, \xi) = \psi_R^{el,vol}(c_{F_R}, \boldsymbol{E}^{e^v}) + \psi_R^{el,iso}(c_{F_R}, \boldsymbol{E}^{e^i}) + \psi_R^{in}(c_{F_R}, \boldsymbol{E}^e - \xi) \,, \tag{54}$$

where $\boldsymbol{E}^e$ depends on $\boldsymbol{E}$ via Eq. (8). Considering the rheological model of Maxwell, for which we refer to Simo and Hughes (1998) or Holzapfel (2001), the inelastic part of the free energy is defined in such a way that

$$\frac{\partial \psi_R^{in}}{\partial \boldsymbol{E}} = -\frac{\partial \psi_R^{in}}{\partial \xi} \,. \tag{55}$$

Provided that the above holds, the selection for ψ_R^{el} and ψ_R^{in} is arbitrary. The elastic reversible behavior occurs once the viscous effects vanish (ideally at $t \to \infty$) and is described by ψ_R^{el}. The inelastic free energy accounts for the non-equilibrium response due to viscosity. By thermodynamic restrictions (47a), (50a), (49) and identity (55), the following identities hold

$$\chi = -\frac{\partial \psi_R^{in}}{\partial \xi} = \frac{\partial \psi_R^{in}}{\partial \boldsymbol{E}} \,, \tag{56a}$$

$$\boldsymbol{S} = \frac{\partial \psi_R^{el}}{\partial \boldsymbol{E}} + \chi \,. \tag{56b}$$

According to Eq. (56b), tensorial internal forces χ can be interpreted as a *non-equilibrium stress tensor* of second Piola-Kirchhoff kind, that accounts for the viscous response.

Following (49) and the Onsager reciprocal relation for the inelastic internal entropy production, a positive definite operator $\mathbb{L}$ is chosen, in such a way that

$$\chi = \mathbb{L}\,\frac{\partial \boldsymbol{\xi}}{\partial t}. \tag{57}$$

7.2. Chemical potentials

Following Serpelloni et al. (2021), the free energy density for the continuum approximation of mixing reads

$$\begin{aligned}\psi_R^{diff}(c_{G_R}, c_{F_R}) = \mu_G^0\, c_{G_R} + R\,T\,c_{G_R}^{max}\left[\vartheta_{G_R}\ln\vartheta_{G_R} + (1-\vartheta_{G_R})\ln(1-\vartheta_{G_R})\right] + \\ + \mu_F^0\, c_{F_R} + R\,T\,c_{F_R}^{max}\left[\vartheta_{F_R}\ln\vartheta_{F_R} + (1-\vartheta_{F_R})\ln(1-\vartheta_{F_R})\right].\end{aligned} \tag{58}$$

Using the thermodynamic restrictions (47b) and (47c) and following the additive decomposition of the Helmholtz free energy (53), the chemical potential of species $a = G, F$ can be written as

$$\mu_G = \frac{\partial \psi_R^{diff}}{\partial c_{G_R}}\,, \tag{59a}$$

$$\mu_F = \frac{\partial \psi_R^{diff}}{\partial c_{F_R}} + \frac{\partial \psi_R^{el,vol}}{\partial c_{F_R}} + \frac{\partial \psi_R^{el,iso}}{\partial c_{F_R}} + \frac{\partial \psi_R^{in}}{\partial c_{F_R}}\,, \tag{59b}$$

where mechanical contributions enter only the definition of chemical potential of the F-actin network. The volumetric contribution $\psi_R^{el,vol}$ affects chemical potential μ_F via the swelling tensor $\boldsymbol{E}^{e^v}$, while $\boldsymbol{E}^{e^i}$ is independent of the concentration of species.

For the simple case of G-actin, the gradient of μ_G reads

$$\mathrm{Grad}\left[\,\mu_G\,\right] = \frac{R\,T}{c_{G_R}^{max}}\,\frac{1}{\vartheta_{G_R}(1-\vartheta_{G_R})}\,\mathrm{Grad}\left[\,c_{G_R}\,\right]\,, \tag{60}$$

and taking advantage of Eq. (51a), (52a), (60) and (59a), the Fick's constitutive relation is obtained

$$\vec{H}_G = -\mathfrak{D}_{G_R}\,\mathrm{Grad}\left[\,c_{G_R}\,\right]\,, \tag{61}$$

where $\mathfrak{D}_{G_R} = \mathfrak{u}_R\,R\,T$ represents G-actin *diffusivity*. Following Eq. (58), (60) and (59b), Eq. (51b) reads

$$\vec{H}_F = -\mathfrak{K}_{F_R}\,\mathrm{Grad}\left[\,c_{F_R}\,\right] - \boldsymbol{M}_{F_R}\,\mathrm{Grad}\left[\,\frac{\partial \psi_R^{el,vol}}{\partial c_{F_R}}\,\right] - \boldsymbol{M}_{F_R}\,\mathrm{Grad}\left[\,\frac{\partial \psi_R^{el,iso}}{\partial c_{F_R}}\,\right] - \boldsymbol{M}_{F_R}\,\mathrm{Grad}\left[\,\frac{\partial \psi_R^{in}}{\partial c_{F_R}}\,\right]\,, \tag{62}$$

where $\mathfrak{K}_{F_R}$ is a term that accounts for the F-actin network transport.

8. Governing equations with boundary conditions. Weak form

Combining the mass action law and the constitutive equations with the mass balance of species and the balance of momentum respectively, the equations that govern all the processes are derived. Taking advantage of Eq. (29), the transport of actin is coupled with polymerization and depolymerization reactions in the mass balance equations

$$\frac{\partial c_{G_R}}{\partial t} + \mathrm{Div}\left[\,\vec{H}_G\,\right] + k_{f_R}\,\frac{\vartheta_{G_R}}{1-\vartheta_{G_R}} - k_{b_R}\,\frac{\vartheta_{F_R}}{1-\vartheta_{F_R}} = s_{G_R}\,, \tag{63a}$$

$$\frac{\partial c_{F_R}}{\partial t} + \mathrm{Div}\left[\,\vec{H}_F\,\right] - k_{f_R}\,\frac{\vartheta_{G_R}}{1-\vartheta_{G_R}} + k_{b_R}\,\frac{\vartheta_{F_R}}{1-\vartheta_{F_R}} = 0 \tag{63b}$$

with $\vec{H}_G$ and $\vec{H}_F$ from Eq. (61) and (62). The balance of linear momentum (22) can be specified as

$$\mathrm{Div}\,[\,\boldsymbol{F}\,\boldsymbol{S}\,] + \vec{B} = \frac{\mathrm{d}\,\rho_{F_R}\,\dot{\vec{X}}}{\mathrm{d}t}\,, \qquad \vec{X} \in \Omega_R\,, \tag{64}$$

where the second Piola–Kirchhoff stress emanates from (47a) and

$$\boldsymbol{F} = (\,1 + c_{F_R}\,\Omega_F\,)^{\frac{1}{3}}\,\boldsymbol{F}^e. \tag{65}$$

Boundary conditions along Neumann boundaries $\partial^N\Omega_R$ read

$$\vec{H}_G \cdot \vec{N} = \overline{h}_{G_R} \qquad \vec{X} \in \partial^N\Omega_R\,, \tag{66a}$$

$$\vec{H}_F \cdot \vec{N} = \overline{h}_{F_R} \qquad \vec{X} \in \partial^N\Omega_R\,, \tag{66b}$$

$$\boldsymbol{P}\,\vec{N} = \overline{\vec{T}} \qquad \vec{X} \in \partial^N\Omega_R\,, \tag{66c}$$

and Dirichlet boundary conditions along $\partial^D\Omega_R$ are

$$c_{G_R} = \overline{c}_{G_R} \qquad \vec{X} \in \partial^D\Omega_R\,, \tag{67a}$$

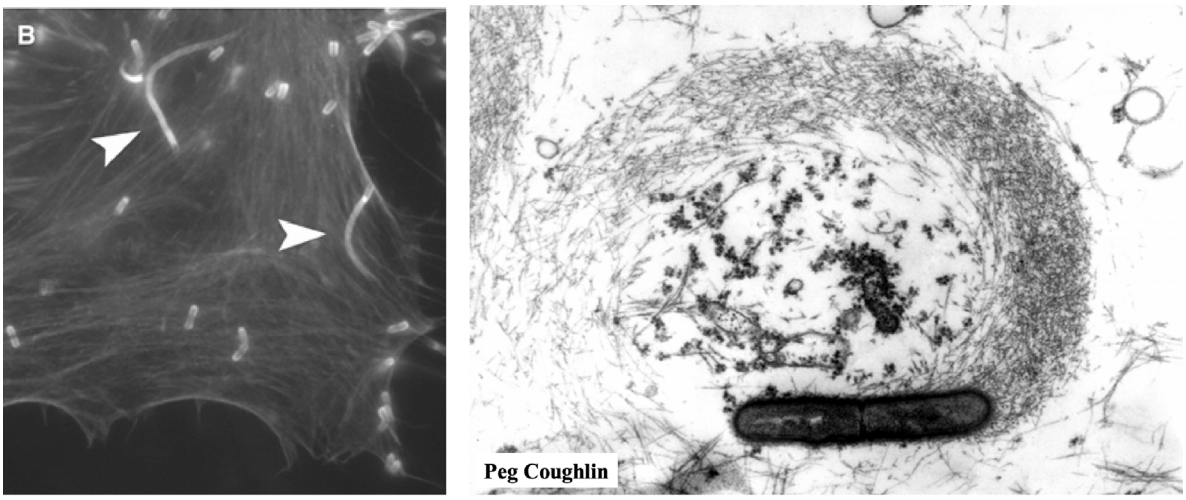

Fig. 3. (a): Movement of Listeria monocytogenes in a cell (Pust et al., 2005). (b): Bacterial surface proteins cause local nucleation of actin filaments (Anon, 2015).

$$c_{F_R} = \overline{c}_{F_R} \qquad \vec{X} \in \partial^D \Omega_R \,, \tag{67b}$$

$$\vec{U}(\vec{X}, t) = \overline{\vec{U}} \qquad \vec{X} \in \partial^D \Omega_R. \tag{67c}$$

The associated initial conditions of Eq. (63) for concentrations, $c_{G_R}(\vec{X}, t = 0)$ and $c_{F_R}(\vec{X}, t = 0)$, as well as for displacements and velocities, $\vec{U}(\vec{X}, t = 0)$ and $\dot{\vec{\chi}}(\vec{X}, t = 0)$, are imposed.

Multiplying by arbitrary test functions $\hat{\mu}_G$, $\hat{\mu}_F$, $\hat{\vec{v}}$ that are homogeneous at the Dirichlet boundaries (Quarteroni and Valli, 1997) and integrating upon the domain Ω_R, the weak forms of governing Eq. (63) and (64) are found

$$\int_{\Omega_R} \hat{\mu}_G \left\{ \frac{\partial c_{G_R}}{\partial t} + \mathrm{Div}\left[\vec{H}_G\right] + w_R^{(16)} - s_{G_R} \right\} + \hat{\mu}_F \left\{ \frac{\partial c_{F_R}}{\partial t} + \mathrm{Div}\left[\vec{H}_F\right] - w_R^{(16)} \right\} + \tag{68}$$

$$+ \hat{\vec{v}} \cdot \left\{ \mathrm{Div}\left[\boldsymbol{P}\right] + \vec{B} - \frac{\mathrm{d}\,\rho_{F_R}\,\ddot{\vec{\chi}}}{\mathrm{d}t} \right\} \mathrm{d}v_R = 0.$$

Using the Gauss theorem, Eq. (68) becomes

$$\int_{\Omega_R} \left(\hat{\mu}_G \frac{\partial c_{G_R}}{\partial t} + \mathrm{Grad}\left[\hat{\mu}_G\right] \cdot \vec{H}_G + \hat{\mu}_G\, w_R^{(16)} - \hat{\mu}_G\, s_{G_R} \right) \mathrm{d}v_R - \int_{\partial^N \Omega_R} \hat{\mu}_G\, \overline{h}_{G_R}\, \mathrm{d}\Gamma + \tag{69}$$

$$+ \int_{\Omega_R} \left(\hat{\mu}_F \frac{\partial c_{F_R}}{\partial t} + \mathrm{Grad}\left[\hat{\mu}_F\right] \cdot \vec{H}_F - \hat{\mu}_F\, w_R^{(16)} \right) \mathrm{d}v_R - \int_{\partial^N \Omega_R} \hat{\mu}_F\, \overline{h}_{F_R}\, \mathrm{d}\Gamma +$$

$$+ \int_{\Omega_R} \left(\hat{\vec{v}} \cdot \vec{B} - \hat{\vec{v}} \cdot \frac{\mathrm{d}\,\rho_{F_R}\,\ddot{\vec{\chi}}}{\mathrm{d}t} - \mathrm{Grad}\left[\hat{\vec{v}}\right] \cdot \boldsymbol{P} \right) \mathrm{d}v_R + \int_{\partial^N \Omega_R} \hat{\vec{v}} \cdot \overline{\vec{T}}\, \mathrm{d}\Gamma \,,$$

where boundary conditions (66) are used in the integrals on the boundary.

9. Actin-based motility of bacterial pathogens

Since cellular motility must account for several elements of the cytoskeletal machinery, we verify the consistency of the chemo-mechanical engine depicted in the former sections on a simpler system, i.e., the motion of non flagellated bacteria through the cytosol. This problem has been largely investigated in the literature (Goldberg, 2001; Ortega et al., 2019; Lamason and Welch, 2017; Choe and Welch, 2016; Pantaloni et al., 2001; Cameron et al., 2000). Nevertheless, some of the material parameters required by our model appear not to be currently available. For this sake, we opened an experimental campaign to validate the model against real bacteria: outcomes will be published. In this section, we limited ourselves to a proof of concept, with data summarized in Table 2.

The polymeric network of F-actin regulates a variety of cellular functions and is a critical target of several intracellular bacterial pathogens (Lamason and Welch, 2017), e.g., *Listeria monocytogenes, Shigella, Ricketssia, Mycobacterium*, and *Burkholderia*. They exploit and manipulate F-actin network at multiple stages of infection to support their survival and growth in the host cell environment. Because of its low virulence and its ease in experimental handling (Cameron et al., 2000), mainly *Listeria monocytogenes* was chosen to

Table 2
Material parameters and other data for the numerical simulations.

Parameter	Symbol	Value	Units	Reference
Forward reaction rate parameter	k_f^*	10.00	$[s^{-1}]$	Raz-Ben Aroush et al. (2017)
Backward reaction rate parameter	k_b^*	0.25	$[s^{-1}]$	Raz-Ben Aroush et al. (2017)
Delay time	τ	30.00	[s]	Cameron et al. (2000)
Length of influence of the signal	ℓ	1.00	[μm]	arbitrary
Signal intensity parameter	α	0.002	[−]	arbitrary
G-actin diffusivity	$\mathbb{D}_{G_R}$	3.00	$[\mu m^2\ s^{-1}]$	Kiuchi et al. (2011)
F-actin network diffusivity	$\mathbb{K}_{F_R}$	0.01	$[\mu m^2\ s^{-1}]$	arbitrary
Equilibrium temperature	T	310.15	[K]	Damioli et al. (2017)
Gas constant	R	8.31	$[J\ K^{-1}\ mol^{-1}]$	–
F-actin network Young Modulus	E	500.00	[Pa]	Chen et al. (2020)
F-actin network Shear Modulus	G	200.00	[Pa]	Chen et al. (2020)
Molar volume of G-actin	ω_G	32.20	$[l\ mol^{-1}]$	Quirion and Gicquaud (1993)
Molar volume of F-actin network	ω_F	58.00	$[l\ mol^{-1}]$	arbitrary
Viscous constant	ν	$3.00\ 10^{-3}$	[Pa s]	Mogilner A (1996)
G-actin initial concentration	$c_{G_R}(X,0)$	2420.00	[μM]	Raz-Ben Aroush et al. (2017)
F-actin network initial concentration	$c_{F_R}(X,0)$	0.00	[μM]	–
Initial displacement	$U_1(X,0)$	0.00	[μm]	–

investigate this form of actin-based motility, with the result of a wider experimental literature compared to other pathogens (Robbins et al., 1999; McGrath et al., 2003; Lacayo and Theriot, 2004; Talman et al., 2014; Costa et al., 2019).

The biochemical processes occurring in the cell during pathogen invasion must link with the formation and dissociation of actin filaments, as well as the associated bacterium displacement. In the following sections, we summarize the model assumptions and the basic phenomena that we have taken into account.

9.1. Basic phenomena and model assumptions

In the suspended resting state, the actin monomers are immersed in the cell cytosol. After the pathogen enters the cytosol, the polymerization of actin monomers at the surface of the bacterium tail generates the *actin comet tail*. It extends mainly along one direction, therefore we simplify the actin-based motility of bacterium as a one dimensional problem.

The polymerization of G-actin is induced by a cascade of signaling pathways triggered by a stable protein on the surface of the bacterium. The precise details of the signaling processes are ignored. Rather, the activity that triggers the formation of the actin comet tail is considered via an activation signal constantly emitted at the bacterium tail. Following Eq. (31), we define the signal $C(\vec{X},t)$ as

$$C(X) = \alpha \cdot \frac{X - s_{signal}}{\ell} \cdot \mathcal{H}(X - s_{signal}) \cdot \mathcal{H}(s_{base} - X)\,, \tag{70}$$

where α is a parameter that is related to the signal strength, s_{base} is the position of the bacterium tail and $\ell = s_{base} - s_{signal}$ is the length of influence of the signal (see Fig. 4). The bacterium tail is located by definition as the first position from the right in which the F-actin network concentration is greater than 0. At initial time $t = 0\,$s, it is set to $s_{base} = 10\ \mu$m.

We neglect the internal generation of G-actin, i.e. $s_{G_R} = 0$. Moreover, we consider a dilute solution, i.e. the mass action law (29) becomes

$$w_R^{(16)} = k_f\, c_{G_R} - k_b\, c_{F_R}\,.$$

The governing equation of linear momentum (64) for pathogens motility can be rephrased as

$$\mathrm{Div}\,[\,\boldsymbol{F}\,\boldsymbol{S}\,] + \vec{B} = M_F\,\frac{\mathrm{d}\,c_{F_R}\,\dot{\vec{\chi}}}{\mathrm{d}t}\,, \tag{71}$$

with M_F representing the molar mass of the F-actin network. We assume that M_F is small, so that the inertial effects are second-order and can be neglected.

Therefore, taking advantage of all previous assumptions, the set of balance Eqs. (63) and (64) for the case of actin-based motility of a bacterium is rewritten as follows:

$$\frac{\partial c_{G_R}}{\partial t} + \mathrm{Div}\left[\,\vec{H}_G\,\right] + k_f\, c_{G_R} - k_b\, c_{F_R} = 0\,, \tag{72a}$$

$$\frac{\partial c_{F_R}}{\partial t} + \mathrm{Div}\left[\,\vec{H}_F\,\right] - k_f\, c_{G_R} + k_b\, c_{F_R} = 0\,, \tag{72b}$$

$$\mathrm{Div}\left[\,P_{11}\,(F_{11})\,\right] + \vec{B} = 0. \tag{72c}$$

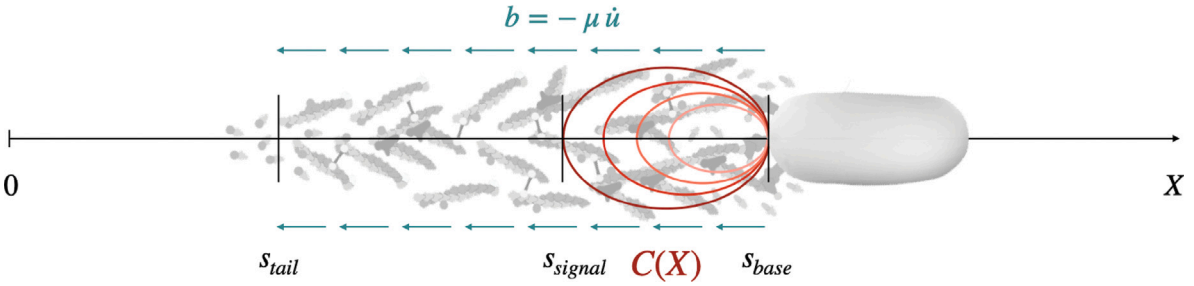

Fig. 4. Schematic representation of actin-based motility model.

Bacteria associated with comet tails move very rapidly within the host cytoplasm, at rates of up to 1 μm/s (Cameron et al., 2000). Considering the bacterium speed, we assume that viscous effects do not have sufficient time to develop in the *actin comet tail*, even if in reality some cross-link rearrangement can occur. For this reason, tensorial internal forces χ are null and Eq. (62) becomes

$$\vec{H}_F = -\mathbb{K}_{F_R}\,\mathrm{Grad}\left[c_{F_R}\right] - \boldsymbol{M}_{F_R}\,\mathrm{Grad}\left[\frac{\partial \psi_R^{el,vol}}{\partial c_{F_R}}\right] - \boldsymbol{M}_{F_R}\,\mathrm{Grad}\left[\frac{\partial \psi_R^{el,iso}}{\partial c_{F_R}}\right]. \tag{73}$$

We consider an elastic strain–energy function ψ_e for Saint-Venant materials in the intermediate configuration

$$\psi_e = \frac{\lambda}{2}\,\mathrm{tr}\left[\boldsymbol{E}^e\right]^2 + \mathrm{G}\,\boldsymbol{E}^e \cdot \boldsymbol{E}^e\ . \tag{74}$$

Using Eqs. (9) and (47a), together with the volumetric transformation of the *Helmholtz free energy*

$$\psi_R^{el} = J^c\ \psi_e\ ,$$

we can derive the stress tensor $\boldsymbol{S}$ making use of identity (8):

$$\boldsymbol{S} = \left.\frac{\partial \psi_R}{\partial \boldsymbol{E}}\right|_{c_{G_R}, c_{F_R}, \xi} = \left.\frac{\partial (J^c\,\psi_e)}{\partial \boldsymbol{E}}\right|_{c_{G_R}, c_{F_R}, \xi} = J^c\ \frac{\partial \psi_e}{\partial \boldsymbol{E}^e}\,\frac{\partial \boldsymbol{E}^e}{\partial \boldsymbol{E}}\bigg|_{c_{G_R}, c_{F_R}, \xi} = J^{c\,1/3}\,\boldsymbol{S}^e\ , \tag{75}$$

with $\boldsymbol{S}^e$ defined as

$$\boldsymbol{S}^e = \frac{\partial \psi_e}{\partial \boldsymbol{E}^e} = \lambda\,\mathrm{tr}\left[\boldsymbol{E}^e\right]\mathbb{1} + 2\,\mathrm{G}\,\boldsymbol{E}^e. \tag{76}$$

In a first approximation, we neglect the dependency of the shear modulus G and Lamè's first parameter λ on the concentration of the F-actin network $\mathrm{G}(c_{F_R})$, $\lambda(c_{F_R})$ and we take them as constant. Accordingly, Eq. (73) becomes

$$\vec{H}_F = -\mathbb{K}_{F_R}\,\mathrm{Grad}\left[c_{F_R}\right] - \boldsymbol{M}_{F_R}\,\mathrm{Grad}\left[\frac{\partial \psi_R^{el}}{\partial c_{F_R}}\right]. \tag{77}$$

The cytoplasmatic fluid in which the F-actin network is immersed is accounted for through external viscous drag shear forces acting on the *actin comet tail*. In one dimensional problems, those shear forces become bulk forces $\vec{B}$. Experimental observations (McGrath et al., 2003) of the *Listeria monocytogenes* moving through the fluid show that turbulence effects can be neglected and it can be considered a purely laminar Stokes' drag. The bulk forces due to the viscous drag are thus taken as proportional to velocity

$$B = -\nu\,\dot{U}_1\ , \tag{78}$$

where ν generally depends on the material properties, the geometry of the object, and the properties of the fluid. In a first approximation, we take ν as a constant.

9.2. Governing equations and boundary conditions

The governing equations read

$$\frac{\partial c_{G_R}}{\partial t} - \frac{\partial}{\partial X}\left[\mathbb{D}_{G_R}\,\frac{\partial c_{G_R}}{\partial X}\right] + k_f\,c_{G_R} - k_b\,c_{F_R} = 0\ , \tag{79a}$$

$$\frac{\partial c_{F_R}}{\partial t} - \frac{\partial}{\partial X}\left[\mathbb{K}_{F_R}\,\frac{\partial c_{F_R}}{\partial X}\right] + \frac{\mathbb{K}_{F_R}\,\Omega_F\,(\mathrm{G}+\frac{\lambda}{2})}{4\,\mathrm{R}\,\mathrm{T}}\,\frac{\partial}{\partial X}\left[c_{F_R}\,\frac{\partial}{\partial X}\left[3\left(\frac{J}{J^c}\right)^4 - 2\left(\frac{J}{J^c}\right)^2\right]\right] + \\ - k_f\,c_{G_R} + k_b\,c_{F_R} = 0\ , \tag{79b}$$

$$\frac{\partial}{\partial X}\left[J^{c^{-1}}\left(1+\frac{\partial U_1}{\partial X_1}\right)\left(J^{c^{-2}}\left(1+\frac{\partial U_1}{\partial X_1}\right)^2-1\right)\right]-\frac{\nu}{\mathrm{G}+\frac{\lambda}{2}}\frac{\partial U_1}{\partial t}=0\,, \tag{79c}$$

with J^c from Eq. (25).

At the initial time $t = 0\,\mathrm{s}$, we assume that: (i) the displacements vanish throughout the stress-free body

$$U_1(X,0)=0\,; \tag{80}$$

(ii) the G-actin concentration is uniform[2] and that no F-actin network exists

$$c_{G_R}(X,0)=2420\ \mu\mathrm{M}\,, \tag{81a}$$

$$c_{F_R}(X,0)=0\ \mu\mathrm{M}. \tag{81b}$$

The cellular domain boundaries are defined on $a = 0\,\mu\mathrm{m}$ and $b = 52\,\mu\mathrm{m}$. The boundary conditions for the *actin comet tail* are prescribed on its front, s_{base}, and its back, s_{tail}, taken as the first position from the left in which the F-actin network concentration is greater than 0. The concentration of G-actin is considered to be constant on the boundaries, in accordance with the initial condition

$$c_{G_R}(a,t)=c_{G_R}(b,t)=c_{G_R}(X,0)\qquad \forall t\in[\,0,t_{end}\,]. \tag{82}$$

We consider a zero flux of F-actin network across the cell boundaries

$$h_{F_R}(a,t)\cdot n_R=h_{F_R}(b,t)\cdot n_R=0\qquad \forall t\in[\,0,t_{end}\,]. \tag{83}$$

The mass of the bacterium is considered to be negligible, therefore at s_{base} a null Neumann condition is imposed. On the back boundary of the *actin comet tail*, bacterium displacement vanish coherently with a steady cellular cytosol, i.e.

$$U_1(s_{tail},t)=0\qquad \forall t\in[\,0,t_{end}\,]\,, \tag{84a}$$

$$P_{11}(s_{base},t)\cdot n_R=0\qquad \forall t\in[\,0,t_{end}\,]. \tag{84b}$$

The parameters chosen for numerical simulations are summarized in Table 2, together with bibliographic references. The forward reaction constant in Eq. (31) has been taken from Raz-Ben Aroush et al. (2017) and amounts at $k_f^* = 10.00\,\mathrm{s}^{-1}$. The backward reaction rate parameter has been set to $k_b^* = 0.25\,\mathrm{s}^{-1}$, consistent with the *severing parameter r* in Raz-Ben Aroush et al. (2017). The average lifetime of actin filaments is $\tau = 30\,\mathrm{s}$ seconds in actin comet tails (Cameron et al., 2000), while it ranges from 20 s to 2 min in lamellipodia.

The diffusivity of G-actin is assumed to be $\mathbb{D}_{G_R} = 3.00\,\mu\mathrm{m}^2\ \mathrm{s}^{-1}$, consistent with the values reported in Kiuchi et al. (2011) that range from 3 to 30 $\mu\mathrm{m}^2\ \mathrm{s}^{-1}$. The transport parameter of the F-actin network $\mathbb{K}_{F_R}$ is supposed to be orders of magnitude smaller than the G-actin counterpart. The length of influence of the signal $\ell = 1.00\,\mu\mathrm{m}$, the signal strength $\alpha = 0.002$ and $\mathbb{K}_{F_R} = 0.01\,\mu\mathrm{m}^2\ \mathrm{s}^{-1}$ have been calibrated in order to obtain a final actin comet tail length of 10 μm, as described in Mogilner A (1996).

The equilibrium temperature is assumed to be $\mathrm{T} = 310\,\mathrm{K}$ (Damioli et al., 2017). In accordance with Chen et al. (2020), the actin polymeric network is characterized by a Young's modulus $\mathrm{E} = 0.50\,\mathrm{kPa}$ and a shear modulus $\mathrm{G} = 0.20\,\mathrm{kPa}$. The molar volume of G-actin has been measured in Quirion and Gicquaud (1993) as $32.20\pm0.21\ \mathrm{mol}^{-1}$. The cytosol viscosity is taken as $\nu = 3.00\cdot10^{-3}\,\mathrm{Pa\ s}$, consistent with Mogilner A (1996). The molar volume of F-actin network was calibrated in order to obtain a bacterium velocity about 1 $\mu\mathrm{ms}^{-1}$.

9.3. Results and discussion

The numerical solution of the problem (79) stems from a semi-discrete Galerkin approximation of its weak form, which can be derived with the same path of reasoning that led to Eq. (69). The unknown fields c_{G_R}, c_{F_R}, and U_1 have been approximated as a product of linear shape functions in space and nodal unknowns that depend solely on time (see Serpelloni et al., 2022 for details). Proper time advancing schemes have been set forth: we make use of an implicit Euler method, considering a uniform time increment. A Newton–Raphson integration scheme has been implemented to solve the non-linear system of equations at each time step. The geometry is tessellated using isoparametric finite elements. Outcomes have been obtained by coding the numerical strategies described above in MATLAB, without relying on level set moving boundary tracking methods.

G and F-actin network concentrations distributions. In Fig. 5 the concentration of G-actin and F-actin network are plotted at several times.

At initial time, the concentration of G-actin is uniform and the concentration of polymerized network is null throughout the domain. The bacterium tail is located out to $s_{base} = 10\,\mu\mathrm{m}$ and so is the signal.

[2] Data of Raz-Ben Aroush et al. (2017) allow to establish the initial concentration of G-actin, taken as the sum of the four actin subpopulations concentrations ($F = 800\ \mu\mathrm{M}$, $f = 400\ \mu\mathrm{M}$, $G = 1200\ \mu\mathrm{M}$, $g = 20\ \mu\mathrm{M}$, see Raz-Ben Aroush et al. (2017)).

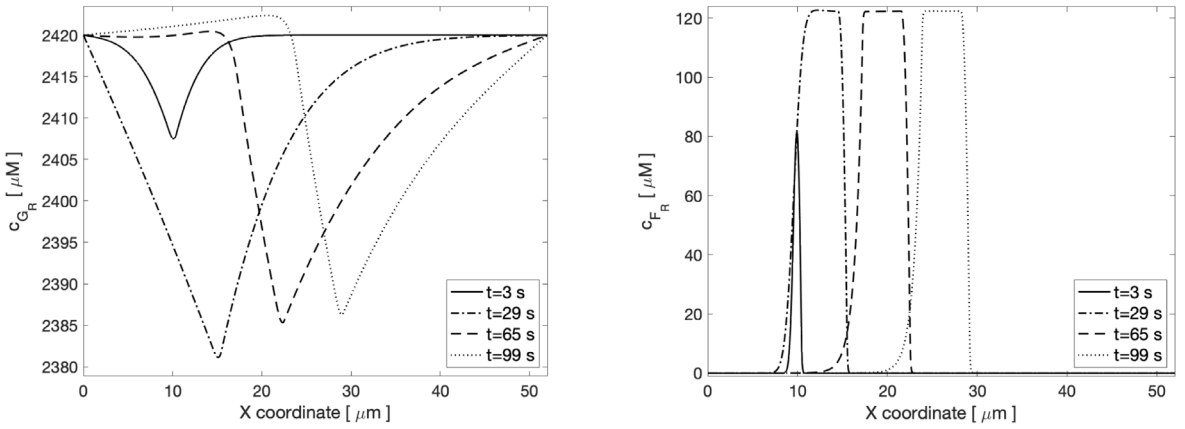

(a) Concentration of G-actin $c_{G_R}(X,t)$. (b) Concentration of F-actin network $c_{F_R}(X,t)$.

Fig. 5. Concentrations of monomer actin and actin network at time $t = 3\,\text{s}$, $t = 29\,\text{s}$, $t = 65\,\text{s}$, $t = 99\,\text{s}$.

At time $t = 3\,\text{s}$, an incipient F-actin network develops in proximity to the signal (see the continuous line in Fig. 5(b)), while the G-actin concentration decreases (see the continuous line in Fig. 5(a)). Filaments polymerize at the bacterial surface to generate force. Far from there, the concentration profiles are unaltered.

At time $t = 29\,\text{s}$, the comet tail is almost completely formed. The dot-dashed line in Fig. 5(b) shows how the network concentration reaches the maximum value $122.28\,\mu\text{M}$, increasing sharply at the leading edge of the bacterium tail. The polymerization of F-actin network moves the bacterium rightward, where the G-actin reaches a minimum (see Fig. 5(a)). The F-actin network does not depolymerize, yet, since $t < \tau$.

At time $t = 65\,\text{s}$, the depolymerization is in place and two parts of the actin comet tail can be devised consistent with the picture in Fig. 3(b). The *head*, close to the signal, is characterized by a dense network of filaments, some of which have just been polymerized. The *back* consists of depolymerizing filaments whose lifetime has been exceeded. The depolymerization of F-actin network in turn induces an increment of G-actin monomers, whose concentration exceeds the initial value at some locations.

As time passes, the length of the actin comet tail and the processes described above become steady. A snapshot at time $t = 99\,\text{s}$ is depicted in Fig. 5. The bacterium moves rightward at constant velocity.

Displacements and Stresses. Fig. 6(a) plots the displacement field $U_1(X)$ at several times. The plots reveal that the polymerization of G-actin into the F-actin network causes a swelling distortion in the domain, which is opposed by the viscous cytosol resistance. The displacements rise as the comet tail develops in time, with a transient process (see $U_1(X)$ at $t = 3\,\text{s}$) until becoming stationary (see $U_1(X)$ at $t = 99\,\text{s}$).

Fig. 6(b) plots the stress $P_{11}(X)$ at several times. From $t = 0\,\text{s}$ to $t = 29\,\text{s}$ the F-actin network is forming and no depolymerization occurs. The body is swelling and the external drag viscous forces cause a compressive state in the F-actin network domain. After $t = \tau$ the F-actin network depolymerizes at the back of the actin comet tail, displacements become nearly stationary in time and so do the stresses. The body is swelling at the front of the actin comet tail, where new F-actin network is forming, and it is shrinking at the back of the *actin comet tail*, where filaments depolymerize. The external forces cause a compressive state in the polymerized part of the body and a tensile state in the depolymerized part.

Velocity and retrograde flow. Fig. 7 plots the velocity $v_1(X)$ at several times. The steady state velocity of the front of the pathogen is about $v = 0.18\,\frac{\mu\text{m}}{\text{s}}$, which is consistent with experimental studies on *Listeria monocytogenes* (Shenoy et al., 2007; Cameron et al., 2000).

As depolymerization takes place at $t > \tau$, the velocity profiles in the network show a positive peak at the leading edge and negative values in the rest of the actin comet tail (see Fig. 7).

Experimental studies on *Listeria monocytogenes actin-based motility* highlight that the F-actin network shows a similar behavior. These experimental investigations encompass the spreading phase of the bacterium from cell to cell (Talman et al., 2014; Kuehl et al., 2015). During this phase, the polymerization of the *actin comet tail* in proximity to the hosting cell membrane causes the formation of membrane protrusions, which allow the bacterium to spread in the neighboring cell. In protrusions that display little or no movement, these experiments reveal that, as a result of F-actin network assembly behind the bacterial tail, the whole network is displaced backwards (a backward drift of the actin network) (Talman et al., 2014). This phenomenon is called *actin retrograde flow in protrusions*, in analogy to the actin retrograde flow observed in lamellipodia (Talman et al., 2014). Our numerical simulations suggest that negative velocities in the *actin comet tail* are caused by depolymerization and shrinking of the network at the back of the *actin comet tail* (see Fig. 7).

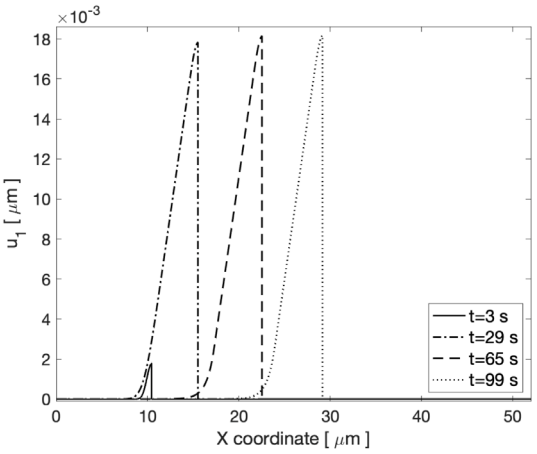

(a) Displacement $U_1\,(X,t)$.

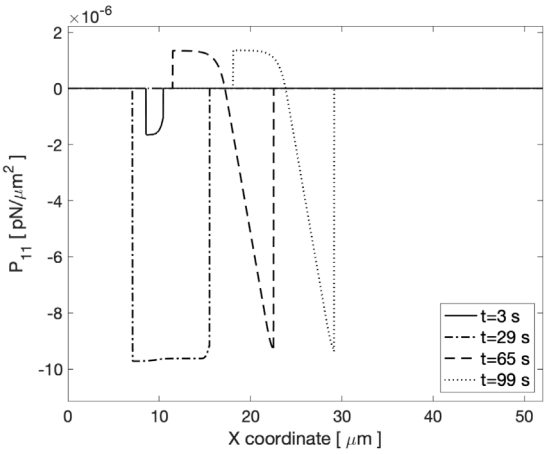

(b) Stress $P_{11}\,(X,t)$.

Fig. 6. Displacements and stresses of actin network at time $t = 3\,\mathrm{s}$, $t = 29\,\mathrm{s}$, $t = 65\,\mathrm{s}$, $t = 99\,\mathrm{s}$.

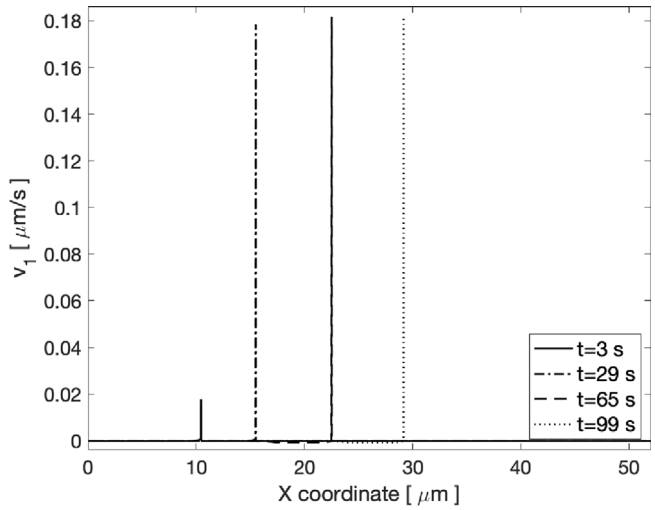

Fig. 7. Velocity $v_1\,(X,t)$ at time $t = 3\,\mathrm{s}$, $t = 29\,\mathrm{s}$, $t = 65\,\mathrm{s}$, $t = 99\,\mathrm{s}$.

10. Concluding remarks

A bio-chemo-mechanical model for actin-based motility of biological systems has been presented. It entails an interaction among external signaling, the elastic response of the polymerized actin network, and the kinetics of the chemical reaction between the monomeric form of G-actin and the network of F-actin. In the proof of concept, it has been shown that the model captures the general features of pathogen motility observed in experimental studies, including the signal dependence of polymerization of F-actin network on the bacterium tail and the F-actin network distribution during pathogen motility.

The model is characterized by some features and assumptions. As highlighted in Fig. 3, filaments in the F-actin network do not seem to be aligned to a preferential direction, rather they form a matrix of arbitrary oriented strands: fibers perpendicular to the tail direction are visible even in the depolymerized zone. For this sake, we did not account for anisotropy in the multiplicative decomposition of the deformation gradient — see Eq. (2). The comet tail evolution is dictated by the motion of the signal, emitted at different positions in time.

We assumed that the maximum number of molecules per unit volume is invariant, i.e. that species in the body occupy a fixed volume and they can relocate in eventual volume expansions of the hosting material. The main consequences of this assumption have been discussed in Serpelloni et al. (2022).

The governing equations depicted in Section 8 hold for any specification of the Helmholtz free energy. In the model of bacterial pathogens motility developed in Section 9 we considered an elastic strain–energy function of Saint-Venant kind, without cross-link protein rearrangement in view of the "high" speed of bacteria in the host cytoplasm. In reality, cross-link reorganization can occur

in pathogens and certainly takes place in cellular motility. More sophisticated, statistically-based continuum theories can be invoked to capture the consequent rate-dependent behavior of the F-actin network upon mechanical loading (Vernerey et al., 2017; Brighenti and Vernerey, 2017). While the consistency of the chemo-mechanical motor has been verified for the bacterial pathogen motility, we limited ourselves to the assumption of material parameters independent of F-actin concentration. To account for the role of concentration in the stiffness of the F-actin network (Chen et al., 2020), further work will be implemented.

The model shall be extended also to account for additional phenomena, such as bacteria invasion of neighboring cells. Cell-to-cell spread via protrusion- and vesicle-mediated transfer can be included by adding models that couple actin-based motility of intracellular bacterial pathogens with the resistance of the membrane, which depends on the trafficking of tension-regulating proteins (Lamason and Welch, 2017). Such developments of the model permit a complete picture of the life cycles of intracellular bacteria that harness actin-based motility.

Moreover, the same polymerization motor can be adapted to describe cellular motility, in angiogenesis or tumor metastasis. The actin polymerization motor operates both in lamellipodia and filopodia at the cellular leading edge. In this case, the model has to take into account all mechanically significant cellular structures involved in the motility, e.g., stress fibers, focal adhesions, microtubules, as well as substrate-cell interactions.

The model can be used to address one of the key challenges in cell biomechanics, namely how to measure the mechanical characteristics of pathogens and cells during actin-based motility. Because the model captures the reorganization of the actin network in response to an external stimulus, it can be used as a framework to design and interpret tailored experiments.

CRediT authorship contribution statement

C. Bonanno: Methodology, Software, Data curation, Validation, Writing – original draft. **M. Serpelloni:** Methodology, Software. **M. Arricca:** Methodology, Discussions. **R.M. McMeeking:** Conceptualization, Writing – review & editing. **A. Salvadori:** Conceptualization, Writing – review & editing, Supervision.

Declaration of competing interest

The authors declare that they have no known competing financial interests or personal relationships that could have appeared to influence the work reported in this paper.

Data availability

No data was used for the research described in the article.

Acknowledgments

Authors express their gratitude to the Ferriera Valsabbia foundation for the generous donation given in order to fund studies in the field of Mechanobiology. This paper has been funded by the Mechanobiology research center at UNIBS (https://www.mechanobiology-unibs.it/) through generous donations of companies *Copan* and *Antares Vision*.

The work has been carried out as part of INdAM (Istituto Nazionale di Alta Matematica) GNFM activities.

Appendix. Proof of eq. (45)

Recalling Eq. (2), (11) and using the identity $\boldsymbol{P} = J\boldsymbol{\sigma}\boldsymbol{F}^{-\mathrm{T}}$, the internal power can be written as

$$
\begin{aligned}
\int_{\mathcal{P}_R} \boldsymbol{P} \cdot \frac{\mathrm{d}\boldsymbol{F}}{\mathrm{d}t}\, \mathrm{d}v_R &= \int_{\mathcal{P}_R} \boldsymbol{S} \cdot \frac{\mathrm{d}\boldsymbol{E}}{\mathrm{d}t}\, \mathrm{d}v_R \\
&= \int_{\mathcal{P}_R} \boldsymbol{P} \cdot \left(\frac{\mathrm{d}\boldsymbol{F}^e}{\mathrm{d}t}\boldsymbol{F}^c + \boldsymbol{F}^e \frac{\mathrm{d}\boldsymbol{F}^c}{\mathrm{d}t}\right) \mathrm{d}v_R \\
&= \int_{\mathcal{P}_R} \boldsymbol{P}\boldsymbol{F}^{c\mathrm{T}} \cdot \frac{\mathrm{d}\boldsymbol{F}^e}{\mathrm{d}t} + \boldsymbol{F}^{e\mathrm{T}}\boldsymbol{P} \cdot \frac{\mathrm{d}\boldsymbol{F}^c}{\mathrm{d}t}\, \mathrm{d}v_R \\
&= \int_{\mathcal{P}_R} \boldsymbol{P}\boldsymbol{F}^{c\mathrm{T}} \cdot \frac{\mathrm{d}\boldsymbol{F}^e}{\mathrm{d}t} + \boldsymbol{F}^{e\mathrm{T}}\boldsymbol{P}\boldsymbol{F}^{c\mathrm{T}} \cdot \boldsymbol{I}^c\, \mathrm{d}v_R \\
&= \int_{\mathcal{P}_R} J\boldsymbol{\sigma}\boldsymbol{F}^{-\mathrm{T}}\boldsymbol{F}^{c\mathrm{T}} \cdot \frac{\mathrm{d}\boldsymbol{F}^e}{\mathrm{d}t} + \boldsymbol{F}^{e\mathrm{T}}J\boldsymbol{\sigma}\boldsymbol{F}^{-\mathrm{T}}\boldsymbol{F}^{c\mathrm{T}} \cdot \boldsymbol{I}^c\, \mathrm{d}v_R \\
&= \int_{\mathcal{P}_C} J^e\boldsymbol{\sigma}\boldsymbol{F}^{e-\mathrm{T}} \cdot \frac{\mathrm{d}\boldsymbol{F}^e}{\mathrm{d}t} + J^e\boldsymbol{F}^{e\mathrm{T}}\boldsymbol{\sigma}\boldsymbol{F}^{e-\mathrm{T}} \cdot \boldsymbol{I}^c\, \mathrm{d}v_c \\
&= \int_{\mathcal{P}_C} \boldsymbol{P}^e \cdot \frac{\mathrm{d}\boldsymbol{F}^e}{\mathrm{d}t} + \boldsymbol{M}^e \cdot \boldsymbol{I}^c\, \mathrm{d}v_c.
\end{aligned}
\tag{A.1}
$$

Taking advantage of Eq. (4), (6), (7), and (46) the Eq. (45) becomes

$$\begin{aligned}\int_{\mathcal{P}_R} \boldsymbol{P} \cdot \frac{\mathrm{d}\boldsymbol{F}}{\mathrm{d}t}\,\mathrm{d}v_R &= \int_{\mathcal{P}_C} \boldsymbol{F}^e\boldsymbol{S}^e \cdot \frac{\mathrm{d}\boldsymbol{F}^e}{\mathrm{d}t} + \boldsymbol{C}^e\boldsymbol{S}^e \cdot \boldsymbol{l}^c\,\mathrm{d}v_c \\ &= \int_{\mathcal{P}_C} \boldsymbol{F}^e\boldsymbol{S}^e \cdot \frac{\mathrm{d}\boldsymbol{F}^e}{\mathrm{d}t} + \boldsymbol{C}^e\boldsymbol{S}^e \cdot \boldsymbol{l}^c\,\mathrm{d}v_c \\ &= \int_{\mathcal{P}_C} \boldsymbol{S}^e \cdot \boldsymbol{F}^{e^{\mathrm{T}}}\frac{\mathrm{d}\boldsymbol{F}^e}{\mathrm{d}t} + \boldsymbol{C}^e\boldsymbol{S}^e \cdot \boldsymbol{l}^c\,\mathrm{d}v_c \\ &= \int_{\mathcal{P}_C} \boldsymbol{S}^e \cdot \frac{\mathrm{d}\boldsymbol{E}^e}{\mathrm{d}t} + \boldsymbol{C}^e\boldsymbol{S}^e \cdot \boldsymbol{d}^c\,\mathrm{d}v_c \\ &= \int_{\mathcal{P}_C} \boldsymbol{S}^e \cdot \frac{\mathrm{d}\boldsymbol{E}^e}{\mathrm{d}t} + \frac{1}{3\boldsymbol{J}^c}\frac{\mathrm{d}\boldsymbol{J}^c}{\mathrm{d}t}\mathrm{tr}\left[\boldsymbol{C}^e\boldsymbol{S}^e\right]\,\mathrm{d}v_c.\end{aligned} \tag{A.2}$$

References

Anon, 2015. Protein polymers, crawling cells and comet tails. https://www.ibiology.org/cell-biology/cell-motility.

Atilgan, E., Wirtz, D., Sun, S.X., 2005. Morphology of the lamellipodium and organization of actin filaments at the leading edge of crawling cells. Biophys. J. 89 (5), 3589–3602.

Bieling, P., Li, T.-D., Weichsel, J., McGorty, R., Jreij, P., Huang, B., Fletcher, D.A., Mullins, R.D., 2016. Force feedback controls motor activity and mechanical properties of self-assembling branched actin networks. Cell 164 (1), 115–127. http://dx.doi.org/10.1016/j.cell.2015.11.057.

Blanchoin, L., Boujemaa-Paterski, R., Sykes, C., Plastino, J., 2014. Actin dynamics, architecture, and mechanics in cell motility. Physiol. Rev. 94 (1), 235–263. http://dx.doi.org/10.1152/physrev.00018.2013.

Borisy, G.G., Svitkina, T.M., 2000. Actin machinery: Pushing the envelope. Curr. Opin. Cell. Biol. 12 (1), 104–112. http://dx.doi.org/10.1016/S0955-0674(99)00063-0, URL https://www.sciencedirect.com/science/article/pii/S0955067499000630.

Brighenti, R., Vernerey, F., 2017. A simple statistical approach to model the time-dependent response of polymers with reversible cross-links. Compos. Part B-Eng. 115, 257–265.

Cameron, L.A., Giardini, P.A., Soo, F.S., Theriot, J.A., 2000. Secrets of actin-based motility revealed by a bacterial pathogen. Nat. Rev. Mol. Cell. Bio. 1 (2), 110–119. http://dx.doi.org/10.1038/35040061.

Carlier, M.-F., Pantaloni, D., 1997. Control of actin dynamics in cell motility. J. Mol. Biol. 269 (4), 459–467. http://dx.doi.org/10.1006/jmbi.1997.1062, URL https://www.sciencedirect.com/science/article/pii/S0022283697910627.

Carlsson, A.E., 2001. Growth of branched actin networks against obstacles. Biophys. J. 81 (4), 1907–1923.

Carlsson, A., 2003. Growth velocities of branched actin networks. Biophys. J. 84 (5), 2907–2918.

Chen, X., Zhu, H., Feng, X., Li, X., Lu, Y., Wang, Z., Rezgui, Y., 2020. Predictive assembling model reveals the self-adaptive elastic properties of lamellipodial actin networks for cell migration. Comm. Biol. 3 (1), 616. http://dx.doi.org/10.1038/s42003-020-01335-z.

Chester, S., Anand, L., 2010. A coupled theory of fluid permeation and large deformations for elastomeric materials. J. Mech. Phys. Solids 58 (11), 1879–1906.

Choe, J.E., Welch, M.D., 2016. Actin-based motility of bacterial pathogens: Mechanistic diversity and its impact on virulence. Pathog. Dis. 74 (8), ftw099. http://dx.doi.org/10.1093/femspd/ftw099.

Costa, A.C., Carvalho, F., Cabanes, D., Sousa, S., 2019. Stathmin recruits tubulin to Listeria monocytogenes-induced actin comets and promotes bacterial dissemination. Cell. Mol. Life Sci. 76 (5), 961–975. http://dx.doi.org/10.1007/s00018-018-2977-7.

Damioli, V., Salvadori, A., Beretta, G., Ravelli, C., Mitola, S., 2017. Multi-physics interactions drive VEGFR2 relocation on endothelial cells. Sci. Rep.-UK 7 (1), 16700.

Deshpande, V.S., McMeeking, R.M., Evans, A.G., 2006. A bio-chemo-mechanical model for cell contractility. Proc. Natl. Acad. Sci. USA 103 (45), 17064–17065.

Ganser, M., Hildebrand, F., Kamlah, M., McMeeking, R., 2019. A finite strain electro-chemo-mechanical theory for ion transport with application to binary solid electrolytes. J. Mech. Phys. Solids 125, 681–713.

Goldberg, M.B., 2001. Actin-based motility of intracellular microbial pathogens. Microbiol. Mol. Biol. R 65 (4), 595–626. http://dx.doi.org/10.1128/MMBR.65.4.595-626.2001, URL https://pubmed.ncbi.nlm.nih.gov/11729265.

Gong, Z., Szczesny, S.E., Caliari, S.R., Charrier, E.E., Chaudhuri, O., Cao, X., Lin, Y., Mauck, R.L., Janmey, P.A., Burdick, J.A., Shenoy, V.B., 2018. Matching material and cellular timescales maximizes cell spreading on viscoelastic substrates. Proc. Natl. Acad. Sci. USA 115 (12), E2686–E2695. http://dx.doi.org/10.1073/pnas.1716620115.

Gong, B., Wei, X., Qian, J., Lin, Y., 2019. Modeling and simulations of the dynamic behaviors of actin-based cytoskeletal networks. ACS Biomater. Sci. Eng. 5 (8), 3720–3734. http://dx.doi.org/10.1021/acsbiomaterials.8b01228.

Gurtin, M., Fried, E., Anand, L., 2010. The Mechanics and Thermodynamics of Continua. Cambridge University Press.

Holzapfel, G., 2001. Nonlinear Solid Mechanics: A Continuum Approach for Engineering. John Wiley & Sons, Ltd..

Hu, L., Papoian, G.A., 2010. Mechano-chemical feedbacks regulate actin mesh growth in lamellipodial protrusions. Biophys. J. 98 (8), 1375–1384. http://dx.doi.org/10.1016/j.bpj.2009.11.054, URL https://pubmed.ncbi.nlm.nih.gov/20409456.

Kadzik, R.S., Homa, K.E., Kovar, D.R., 2020. F-actin cytoskeleton network self-organization through competition and cooperation. Annu. Rev. Cell. Dev. Bi 36 (1), 35–60. http://dx.doi.org/10.1146/annurev-cellbio-032320-094706.

Kang, H., Perlmutter, D.S., Shenoy, V.B., Tang, J.X., 2010. Observation and kinematic description of long actin tracks induced by spherical beads. Biophys. J. 99 (9), 2793–2802. http://dx.doi.org/10.1016/j.bpj.2010.08.058, URL https://pubmed.ncbi.nlm.nih.gov/21044576.

Kiuchi, T., Nagai, T., Ohashi, K., Mizuno, K., 2011. Measurements of spatiotemporal changes in G-actin concentration reveal its effect on stimulus-induced actin assembly and lamellipodium extension. J. Cell. Biol. 193 (2), 365–380. http://dx.doi.org/10.1083/jcb.201101035.

Kuehl, C.J., Dragoi, A.-M., Talman, A., Agaisse, H., 2015. Bacterial spread from cell to cell: Beyond actin-based motility. Trends Microbiol. 23 (9), 558–566. http://dx.doi.org/10.1016/j.tim.2015.04.010, URL https://pubmed.ncbi.nlm.nih.gov/26021574.

Lacayo, C.I., Theriot, J.A., 2004. Listeria monocytogenes actin-based motility varies depending on subcellular location: A kinematic probe for cytoarchitecture. Mol. Biol. Cell. 15 (5), 2164–2175. http://dx.doi.org/10.1091/mbc.e03-10-0747.

Lamason, R.L., Welch, M.D., 2017. Actin-based motility and cell-to-cell spread of bacterial pathogens. Curr. Opin. Cell. Biol. 35, 48–57. http://dx.doi.org/10.1016/j.mib.2016.11.007, URL https://pubmed.ncbi.nlm.nih.gov/27997855.

Le Clainche, C., Carlier, M.-F., 2008. Regulation of actin assembly associated with protrusion and adhesion in cell migration. In: Physiological Reviews. Physiol. Rev. 88 (2), 489–513. http://dx.doi.org/10.1152/physrev.00021.2007.

Li, Y., Bhimalapuram, P., Dinner, A.R., 2010. Model for how retrograde actin flow regulates adhesion traction stresses. J. Phys.-Conden.s Mat. 22 (19), 194113. http://dx.doi.org/10.1088/0953-8984/22/19/194113.

Lin, Y., Shenoy, V.B., Hu, B., Bai, L., 2010. A microscopic formulation for the actin-driven motion of listeria in curved paths. Biophys. J. 99 (4), 1043–1052. http://dx.doi.org/10.1016/j.bpj.2010.06.001.

McGrath, J.L., Eungdamrong, N.J., Fisher, C.I., Peng, F., Mahadevan, L., Mitchison, T.J., Kuo, S.C., 2003. The force-velocity relationship for the actin-based motility of listeria monocytogenes. Curr. Biol. 13 (4), 329–332. http://dx.doi.org/10.1016/s0960-9822(03)00051-4.

Mogilner A, O.G., 1996. Cell motility driven by actin polymerization. Biophys. J. 71 (6), 3030–3045.

Mueller, J., Szep, G., Nemethova, M., de Vries, I., Lieber, A.D., Winkler, C., Kruse, K., Small, J.V., Schmeiser, C., Keren, K., Hauschild, R., Sixt, M., 2017. Load adaptation of lamellipodial actin networks. Cell 171 (1), 188–200.e16. http://dx.doi.org/10.1016/j.cell.2017.07.051, URL https://www.sciencedirect.com/science/article/pii/S0092867417308887.

Murphy, L., Madzvamuse, A., 2020. A moving grid finite element method applied to a mechanobiochemical model for 3D cell migration. Appl. Numer. Math. 158, 336–359.

Ni, H., Papoian, G.A., 2021. Membrane-MEDYAN: Simulating deformable vesicles containing complex cytoskeletal networks. J. Phys. Chem. B 125 (38), 10710–10719. http://dx.doi.org/10.1021/acs.jpcb.1c02336.

Ortega, F.E., Koslover, E.F., Theriot, J.A., Garrett, W.S., Orth, K., Slauch, J., Momeni, B., 2019. Listeria monocytogenes cell-to-cell spread in epithelia is heterogeneous and dominated by rare pioneer bacteria. ELIFE 8, e40032. http://dx.doi.org/10.7554/eLife.40032.

Pantaloni, D., Le Clainche, C., Carlier, M.-F., 2001. Mechanism of actin-based motility. Science 292 (5521), 1502–1506. http://dx.doi.org/10.1126/science.1059975.

Pizarro-Cerdá, J., Kühbacher, A., Cossart, P., 2012. Entry of listeria monocytogenes in mammalian epithelial cells: An updated view. CSH Perspect. Biol. 2 (11), a010009. http://dx.doi.org/10.1101/cshperspect.a010009, URL https://pubmed.ncbi.nlm.nih.gov/23125201.

Pollard, T.D., 2016. Actin and actin-binding proteins. CSH Perspect. Biol. 8 (8), a018226. http://dx.doi.org/10.1101/cshperspect.a018226, URL https://pubmed.ncbi.nlm.nih.gov/26988969.

Pollard, T.D., Borisy, G.G., 2003. Cellular motility driven by assembly and disassembly of actin filaments. Cell 112, 453–465.

Pust, S., Morrison, H., Wehland, J., Sechi, A.S., Herrlich, P., 2005. Listeria monocytogenes exploits ERM protein functions to efficiently spread from cell to cell. Embo. J. 24 (6), 1287–1300. http://dx.doi.org/10.1038/sj.emboj.7600595.

Quarteroni, A., Valli, A., 1997. Numerical Approximation of Partial Differential Equations. Springer Verlag, Berlin.

Quirion, F., Gicquaud, C., 1993. Changes in molar volume and heat capacity of actin upon polymerization. Biochem. J. 295 (3), 671–672. http://dx.doi.org/10.1042/bj2950671, arXiv:https://portlandpress.com/biochemj/article-pdf/295/3/671/612392/bj2950671.pdf.

Radoshevich, L., Cossart, P., 2018. Listeria monocytogenes: Towards a complete picture of its physiology and pathogenesis. Nat. Rev. Microbiol. 16 (1), 32–46. http://dx.doi.org/10.1038/nrmicro.2017.126.

Raz-Ben Aroush, D., Ofer, N., Abu-Shah, E., Allard, J., Krichevsky, O., Mogilner, A., Keren, K., 2017. Actin turnover in lamellipodial fragments. Curr. Biol. 27 (19), 2963–2973.e14.

Robbins, J.R., Barth, A.I., Marquis, H., de Hostos, E.L., Nelson, W.J., Theriot, J.A., 1999. Listeria monocytogenes exploits normal host cell processes to spread from cell to cell. J. Cell. Biol. 146 (6), 1333–1350. http://dx.doi.org/10.1083/jcb.146.6.1333.

Rubinstein, B., Jacobson, K., Mogilner, A., 2005. Multiscale two-dimensional modeling of a motile simple-shaped cell. Multiscale Model. Simul. 3 (2), 413–439.

Serpelloni, M., Arricca, M., Bonanno, C., Salvadori, A., 2021. Modeling cells spreading, motility, and receptors dynamics: A general framework. Acta Mech. Sin. 37 (6), 1013–1030.

Serpelloni, M., Arricca, M., Bonanno, C., Salvadori, A., 2022. Chemo-transport-mechanics in advecting membranes. Int. J. Eng. Sci. 181, 103746.

Shenoy, V.B., Tambe, D.T., Prasad, A., Theriot, J.A., 2007. A kinematic description of the trajectories of Listeria monocytogenes propelled by actin comet tails. Proc. Natl. Acad. Sci. USA 104 (20), 8229–8234. http://dx.doi.org/10.1073/pnas.0702454104.

Simo, J., Hughes, T., 1998. Computational Inelasticity. Springer-Verlag, New York.

Svitkina, T., 2018. The actin cytoskeleton and actin-based motility. CSH Perspect. Biol. 10 (1), a018267. http://dx.doi.org/10.1101/cshperspect.a018267, URL https://pubmed.ncbi.nlm.nih.gov/29295889.

Talman, A.M., Chong, R., Chia, J., Svitkina, T., Agaisse, H., 2014. Actin network disassembly powers dissemination of Listeria monocytogenes. J. Cell. Sci. 127 (1), 240–249. http://dx.doi.org/10.1242/jcs.140038.

Theriot, J.A., 2000. The polymerization motor. TRAFFIC 1 (1), 19–28. http://dx.doi.org/10.1034/j.1600-0854.2000.010104.x.

Vernerey, F., Farsad, M., 2014. A mathematical model of the coupled mechanisms of cell adhesion, contraction and spreading. J. Math. Biol. 68, 989–1022.

Vernerey, F., Long, R., Brighenti, R., 2017. A statistically-based continuum theory for polymers with transient networks. J. Mech. Phys. Solids 107, 1–20.